Doctorate Dissertation

博士論文

Advancement in Normal-Mode Method for Tsunami Computation: Simulation of Tsunami Waveforms and Characterization of Submarine Faults in the Sea of Japan

（津波計算におけるノーマルモード法の発展：津波波形計算と日本海における海底断層の類型化）

A Dissertation Submitted for Degree of Doctor of Philosophy

July 2018

平成 30 年 7 月博士(理学)申請

Department of Earth and Planetary Science, Graduate School of Science,

The University of Tokyo

東京大学大学院理学系研究科地球惑星科学専攻

Yifei Wu

呉　逸飛

ABSTRACT

The normal-mode method (NMM) is widely used in seismology, ocean tide and seiche studies. While most of the former NMM applications to tsunami focused on modal analysis of a bay with incoming waves, Satake and Shimazaki (1987, 1988) proposed a method to simulate tsunami waveforms based on mode superposition, which is considered to be faster than the finite difference method (FDM). They also pioneered to conduct a modal analysis of tsunami source characterization in the Sea of Japan using the NMM, where a tsunami source could be included into the model. However, their proposal was only tested in a simple ideal case which is far from the reality and few properties of NMM simulation were understood. Besides, their source characterization was qualitative due to the coarse grids and the limited number of modes.

To validate NMM in a realistic case and quantitative source characterization, high resolution normal-mode solutions of the Sea of Japan are required. In this study, I first extended the previous NMM into a spherical coordinate system and used an experiential normalization way to simplify the numerical calculation. Then linear matrix storage and matrix-vector multiplication were implemented, and a modern sparse eigenvalue solver was incorporated, which made the calculation of large scale NMM problems realistic. In addition, a parallel version of the calculation was also developed.

These improvements enabled us to obtain 6,000 modal solutions (down to a period of around 8 min) of 2-arc-min grids and 3000 modal solutions (down to around 11.5 min) of 1-arc-min grids for the Sea of Japan. By the superposition of these modes, tsunami waveforms were synthetized by the NMM, for the first time, for the 1983 Sea of Japan earthquake (Mw 7.7). Comparison with the results from the FDM and examination in both time and frequency domains confirmed the validity of the NMM when the modes cover the frequency range of the signal.

Besides the validation of NMM waveform simulation, its properties were carefully examined. Simulation time were compared with FDM and an improvement was proposed so that the time using the NMM may be faster than using the FDM by several orders, which strengthens the advantage of the NMM. In addition, a relationship between the mode order and the mode frequency was proposed so that it is possible to estimate in advance the required number of modes of a given maximum frequency.

I then conducted a novel modal analysis, utilizing the high resolution normal-mode solutions to characterize 60 potential submarine faults in the Sea of Japan. A quantitative mode grouping method using kurtosis was proposed, dividing the obtained 6,000 modes into three types: 622 basin-wide modes, 4,953 regional modes, and 425 local modes.

The excitation weights for the 60 fault models along the eastern margin of the Sea of Japan were computed, which showed that the average excitation was larger for the sources located at shallower water depth or with larger magnitude. Quantitative examinations showed that among the three types of modes, the regional modes distribute their energy more efficiently at a large costal area and therefore contribute the most to the costal tsunamis.

Finally, a symmetric construction way of NMM eigenvalue-problem was proposed, which enabled us to compute 15,000 modes of the Sea of Japan down to 5 min in period. Using these modal solutions, tsunami waveforms synthetized by mode superposition can cover the usual frequency band in the Sea of Japan, which makes it possible to simulate waveforms with high frequency energy. Besides, this approach eliminated the inaccuracy introduced by the experiential mode normalization, resulting almost no energy before the initial arrival and better agreements to FDM around the onset. These improvements further made the NMM a practical tool for the tsunami simulation in the Sea of Japan.

ACKNOWLEDGEMENTS

First, I would like to express my sincere gratitude to my advisor Prof. Kenji Satake for the continuous supervision and support of my Ph.D. study, for his enthusiasm, patience and of course his immense knowledge. And his passion and energy as a researcher are always my example. It is hard to imagine my Ph.D. study without his supporting and encouragement.

Then, I would like to have special thanks to Prof. Shingo Watada for the invaluable hours he spent during my harshest time, also for his deep insights into the essential physics or mathematics of a problem. Many issues are illuminated just after having a discussion with him. I would also like to give special thanks to Prof. Nozomu Takeuchi. The idea and most of the equations of the symmetric NMM problem construction in Section 5.1 are originated from him. And only with this improvement can NMM simulate waveforms with enough modes inside the Sea of Japan.

Besides, I would like to thank the rest of my thesis committee: Prof. Hitoshi Kawakatsu, Prof. Kiwamu Nishida and Prof. Yoshiyuki Tanaka for their insightful comments, but also for the hard question which incentivized me to widen my research from various perspectives.

I thank my lab mates for the stimulating discussions and for all the fun we have had in the last three years. In particular, I thank Yuchen Wang for all aspects of academic discussions, as well as his encouragement. I thank Satoshi Kusumoto for his kindness to my life in Tokyo. I am also grateful to Dr. Virgile Rakoto for appreciating my work as well as many useful discussions, together with the happy&bankrupt days in Tokyo and Paris.

I would also like to thank MEXT for providing me the scholarship to pursue the Ph.D. study.

Last but not the least, I would like to thank my parents for supporting me spiritually throughout writing this thesis.

1 INTRODUCTION

A shallow-water wave theory is usually used to describe the propagation of tsunamis. Because the velocity of small-amplitude shallow-water waves depends only on the water depth, many numerical computations have been made for tsunami propagation. The tsunami numerical computation solves the equations of motion and continuity for shallow-water waves with appropriate boundary and initial conditions. The most common and well-known methods are the finite difference method (FDM) and finite element method (FEM). The normal-mode method (NMM) can also solve these problems, but it is less studied and used, especially in the field of tsunami research. Analytically, the solution of partial differential equations can be expressed by the combination of an infinite number of basis functions, or modes. For given equations, these modes are orthogonal (or "normal") to each other, and together they span the solution space of these equations.

When using a numerical approach, we can obtain only a finite number of modes. Even if we use analytical basis functions, we still cannot use an infinite number, which separates this method from the analytic case. The NMM has an advantage to synthesize any band-limited waveforms by the modal superposition of all finite number of modal solutions within the frequency band. With this advantage the NMM has been extensively used to compute band-limited seismic waveforms from a large number of the modal solutions of the whole Earth. A numerical advantage of the NMM is that, once the modal solutions of a specific area have been calculated and stored inside the

computer, waveforms excited by a given source in this area can be synthesized as a superposition of normal modes, which is an extremely fast process because it consists of only some simple calculations and file input and output. Another point of NMM is that, it can produce information directly in the frequency domain for purpose like modal analysis.

The NMM is often used in geophysics. For example, gravest free oscillations of systems, such as the solid Earth and an ocean basin have been studied using the NMM. The Centroid Moment Tensor Project focal mechanism solution (Dziewonski & Woodhouse, 1983) used modal solutions to synthesize the seismic waveforms. This utilizes the fast superposition property of NMM. Meanwhile, as a frequency domain method, the NMM is also a powerful tool for assessing the resonant oscillations between the atmosphere and the solid earth. For example, Watada and Kanamori (2010) successfully used the NMM to explain the long-period harmonic Rayleigh waves observed during the 1991 Mt. Pinatubo eruption in the Philippines.

Before talking about NMM applied to tsunami researches, it is worthy to mention the development of NMM in the field ocean tides. A series of papers (Platzman, 1978, 1984a, 1984b; Platzman et al., 1981) first proposed a way to construct the eigenvalue-problem of the world ocean from the linear shallow-water equations with Coriolis force and then solved it to obtain the normal-mode solutions for the world ocean in the tidal period range. Müller (2007) further expanded the calculation by incorporating a full loading effect into the calculation. The full loading effect means that the elasticity of the Earth is also considered so that a mass like water column will deform the surface of the earth. This is also an important topic in recent tsunami research (Allgeyer & Cummins, 2014; Watada et al., 2014). For details of these ocean tide topics, see Sanchez (2008). These studies are quite illuminating for tsunami research because they are basically solving similar equations, but in a different frequency band.

NMM applied in the field of tsunami research were mostly motivated by seiche or harbor oscillations (Rabinovich, 2009). The history of using the NMM to study tsunamis may go back to Loomis (1973), who described a novel method for calculating the normal-mode solutions for irregular bodies of water with variable depth. As an application, he used the method to calculate the normal-mode solutions for Honokohau Harbor in Hawaii and discussed its properties (Loomis, 1975). Using Loomis's method,

Aida (1996) obtained the normal-mode solutions for Tokyo Bay to study the properties of the incident tsunami waves inside it. Again using Loomis's method, Takigawa (2015) showed that Tokyo Bay responded differently to different tsunami events.

These tsunami NMM studies focused on modal analysis of (almost) closed bays or basins which are surrounded by the land and artificial nodal lines in the ocean area. A modal solution with large amplitude in a concentrated area can be interpreted as a trapped wave characteristic to the area. Other modal solution with distributed amplitudes in a wide area corresponds to the traveling waves. Many modes have mixed-type wave characteristics between these two types, depending on the location inside the area.

Certainly, modal analysis can be conducted using other methods. Yalciner & Pelinovsky (2007), Bellotti et al. (2012b), and Heidarzadeh & Satake (2014) conducted modal analyses by simply looking at the Fourier amplitude spectrum of observed time domain waveforms. Bellotti et al. (2012a) proposed a novel modal analysis method that can estimate the frequency response of the water body in an area to the input waves coming through the open boundary, by introducing a radiation boundary condition for the open ocean. They identified modes at frequencies with large amplitude response. Their new method can be applied to even a bay surrounded by continental shelf (Bellotti et al., 2012b; Cortés et al. 2017). The amplitude pattern of the gravest modes can be interpreted to understand the physical property of each mode. Notice that their modes are not normal-modes but rather quasi-normal-modes because of the radiation boundary.

While most NMM researches were limited to modal analysis, Satake and Shimazaki (1987) demonstrated by a simple synthetic test that tsunami waveforms for ocean basins with an ideal geometry can be synthesized by a superposition of numerical normal modes obtained by Loomis's method. This was perhaps the first time that numerical normal modes were used to synthesize waveforms. However, their work has two limitations. First, the calculation area is simple: it consists of only 32x16 grids and has uniformed water depth. Second, the source is simple: it is a square uniform rise of water. These limitations made the test far from realistic. Besides, little is known about the property of simulation using MNN: the calculation time, which supposed to be an

advantage of the NMM, was not measured; the relation between the goodness of synthesized waveforms and the modes used was also not clear.

In another paper by Satake & Shimazaki (1988), they obtained the normal-mode solutions for the Sea of Japan and discussed the properties of the tsunamis excited by the 1964 Niigata earthquake and the 1983 Sea of Japan earthquake using the normal-mode excitation weights in the Sea of Japan by these two events. This was a novel modal analysis approach since their NMM calculation area includes these sources, which are not possible for any other frequency domain modal analysis methods. Their modal analysis differs from other modal analysis in one more point: their modal analysis dealt with higher modes in a large region while most of the tsunami modal analysis deal with several leading modes in a small to moderate region. Novel approach requires novel tools, in this case a mode grouping criterion based on the affecting area is needed. However, in their research, they divided the calculated modes into two groups by pure observation. Besides, their modal solution was rather coarse because it contained only 100 modes down to about 50 min and it was obtained from 10 arc-min grids due to computational limitations. (This is also the reason that their modal solution could not be used to simulate tsunami waveforms.)

In this thesis, I further develop the NMM from Satake and Shimazaki's (1987, 1988) ideas to synthesize tsunami waveform and characterize the tsunamis sources based on the NMM.

Section 2 presents the basic methodology and mathematical tools, together with my improvements to enable calculating a high-resolution modal solution, and some new tools. Starting from the linear shallow-water equations, the problem to solve is constructed. Then analytical solution in two ideal cases are shown. Next, the numerical scheme with an experiential mode normalization is introduced and improvements to accelerate the calculation are listed, as well as the parallelization of the calculation. After that, bathymetry data for high-resolution normal-mode solutions are introduced for the Sea of Japan. Besides, a relationship between mode order and mode frequency is proposed and examined. Finally, an automatic method to group modes is described by introducing a statistical value for each eigenfunction. This method is then applied to the Sea of Japan. Part of section 2.2 and part of 2.3 were published in a former research paper (Wu and Satake, 2018).

Section 3 mainly deals with tsunami wave simulation using NMM mode superposition. First with the obtained modal solutions, I successfully synthesize tsunami waveforms excited by the 1983 Sea of Japan earthquake (Mw 7.7), for what I believe to be the first time. Next in both time and frequency domain, the goodness of the simulation results is examined and their reasons are understood. Then a way to estimate the required mode number in order to simulate the tsunami waveform at a given place is given. Finally and most importantly, an improvement of mode superposition is proposed so that the waveform simulation time using NMM may be faster than FDM by several orders even in a moderate region like the Sea of Japan. Section 3.1, part of 3.2 and part of 3.3 were published in a former research paper (Wu and Satake, 2018).

In Section 4, a novel modal analysis is conducted. Tsunami hazards of 60 potential submarine faults in the Sea of Japan are examined by characterizing the tsunami sources with their modal excitation weights. Grouping of the modes are incorporated into this novel modal analysis that includes sources in the calculation domain and that utilizes a large number of modes. Section 4.1, 4.2 and part of 4.3 were published in a former research paper (Wu and Satake, 2018).

In Section 5, a symmetric construction way of NMM eigenvalue-problem in the Sea of Japan in the spherical coordinates is proposed, together with accurate mode normalization and superposition equations. The symmetric approach enables faster calculation of more modal solutions. Then I revisit the same problem in Section 2.3 and 3 and manage to compute 15000 modes down to 5 min in period and simulate tsunami waveforms in the Sea of Japan which better reproduce the observations than these in Section 3.

In Section 6, a way to directly obtain higher modes, other forms of NMM equations as well as the potential of obtaining a NMM solution for the world ocean are discussed.

2 IMPROVED NMM SOLUTIONS AND THEIR PROPERTIES

2.1 Basic Mathematics

2.1.1 Basic Equations

For many tsunami problems, linear shallow equations are the equations to solve:

$$\frac{\partial \boldsymbol{V}}{\partial t} = -g\nabla\eta \quad (2.1a)$$

$$\frac{\partial \eta}{\partial t} = -\nabla \cdot (D\boldsymbol{V}) \quad (2.1b)$$

where $\boldsymbol{V}$ is the velocity vector of the water, η is the sea surface elevation, D is the water depth and g is the gravitational acceleration.

Differentiating both sides of (2.1b) by t and substituting (2.1a) into it, we get:

$$\frac{\partial^2 \eta}{\partial t^2} = \nabla \cdot (gD\nabla\eta) \quad (2.2)$$

Ignoring the change of gravitational acceleration g at difference places, and solve (2.2) using separation of variables, that is to set $\eta(\boldsymbol{x},t)= h(\boldsymbol{x}) \cdot T(t)$, we then obtain:

$$\frac{1}{T}\frac{\partial^2 \mathrm{T}}{\partial t^2} = \frac{g}{h}\nabla \cdot (D\nabla \mathrm{h}) \quad (2.3)$$

Because the left side is a function of only t and the right side is a function of only $\boldsymbol{x}$, the only possibility is that both sides equal to a constant that is irrelevant to either t or $\boldsymbol{x}$. Set the constant to be λ', we obtain two equations:

$$\frac{\partial^2 \mathrm{T}}{\partial t^2} = \lambda' T \quad (2.4a)$$

$$\nabla \cdot (D\nabla h) = \frac{\lambda'}{g} h \quad (2.4b)$$

Solving the first equation (2.4a) will yield solution $T(t) = e^{\pm i\omega \mathrm{t}}$, where $\lambda' = -\omega^2$ and ω is the angular eigen-frequency of the travelling wave. (We do not consider the case that $\lambda'>0$, which corresponds to a solution that the amplitude increases or decreases through time.)

Finally we obtain the same equation of the eigenvalue problem as in Loomis (1973) to solve:

$$\nabla \cdot (D\nabla h) = \lambda h \quad (2.5)$$

where $\lambda = -\frac{\omega^2}{\mathrm{g}}$

In addition to the differential equation, we also need the boundary condition to form a complete problem. There are two kind of boundaries. First is the boundary between water and land. This boundary condition is expressed as $\frac{\partial h}{\partial \boldsymbol{n}} = 0$, where $\boldsymbol{n}$ is unit vector perpendicular to the boundary. Another boundary is the open boundary between the water of calculation area and the water of outside. This boundary condition is expressed as h=0, also called the node boundary. Note that the expression for the first boundary condition is exact. This boundary condition represents a total reflection of waves at the boundary between land and water, which is widely used in other calculation methods like FDM. But the second boundary condition is an approximation. This kind of

boundary is usually expressed by a formula that retains the shape of the water surface as a wave passes through the boundary, which is more physically reasonable. In normal mode approach, this is very hard to realize. Here I chose to use the simple form h=0. Loomis (1973, 1975) has discussed about the validity of this approximation and concluded that the difference is not big against the result of assigning an infinite open sea outside the boundary. Similar results can be found in the case of Marina di Carrara harbour of Belloti et al. (2012b). Besides, for an area like the Sea of Japan, the portion of this node boundary condition is very small, thus we can expect little effect by introducing this kind of boundary condition. But special care should be taken when dealing with something near a node boundary. For example, when synthesizing tsunami waveform, it would better not trust the waveform near a node boundary. Another example is, when dealing with an earthquake source close or even at this kind of boundary, we may get a wrong result. In other words, dealing with something that is too close to a node boundary should be avoided.

So finally the eigenvalue-problem to solve is:

$$\nabla \cdot (D\nabla h) = \lambda h$$

where $\lambda = -\frac{\omega^2}{g}$ and with boundary condition $\frac{\partial h}{\partial \boldsymbol{n}} = 0$ at B_1 and h=0 at B_2. B_1 is the land-ocean boundary and B_2 is the open ocean boundary.

2.1.2 Mode Superposition

The modal solutions have the property of orthogonality, namely:

$$\int h_l(\boldsymbol{x}) h_m(\boldsymbol{x}) d\boldsymbol{x} = \delta_{lm} \qquad (2.6)$$

where δ_{lm} is the Kronecker delta. Equation (2.6) also indicates that the modes are normalized so that their L2-norm equals 1.

Satake and Shimazaki (1987) pointed out that these obtained normal modes can be used to synthesize tsunami waveforms. The sea surface displacement η at any point $\boldsymbol{x}$ and time t can be expressed as a superposition of the normal modes:

$$\eta(\boldsymbol{x}, t) = \sum_l C_l h_l(\boldsymbol{x}) cos\omega_l t \qquad (2.7)$$

where C_l is the excitation weight (or amplitude) for the *l*-th mode and can be obtained from the initial condition:

$$C_l = \int \eta_0(\boldsymbol{x}) h_l(\boldsymbol{x}) d\boldsymbol{x} \qquad (2.8)$$

where $\eta_0(\boldsymbol{x})$ is the initial distribution of the sea surface displacement. Note that the sea surface uplift is assumed to coincide instantly with the earthquake, which is generally a good approximation.

The equation (2.8) can be deduced as following:

The given initial condition $\eta_0(\boldsymbol{x})$ can be represented as

$$\eta_0(\boldsymbol{x}) = \eta(\boldsymbol{x}, t = 0) = \sum_l C_l h_l(\boldsymbol{x})$$

Multiply $h_m(\boldsymbol{x})$ on both sides and integral over $d\boldsymbol{x}$ yields:

$$\int \eta_0(\boldsymbol{x}) h_m(\boldsymbol{x}) d\boldsymbol{x} = \int \sum_l C_l h_l(\boldsymbol{x})\, h_m(\boldsymbol{x}) d\boldsymbol{x}$$

$$= \int \sum_l C_l \delta_{lm}\ d\boldsymbol{x}$$

$$= C_m$$

To calculate the above problem numerically, the spatial functions in equations (2.5), (2.7), and (2.8) need to be discretized. After discretization, equation (2.5) is in the form of a matrix-eigenvalue problem:

$$a_{ij} h_j = \lambda h_i \qquad (2.9)$$

Here, matrix a_{ij} has dimension $n \times n$, where *n* is the total number of the ocean grids.

Then we can solve this problem and obtain eigenvalue λ and its corresponding eigenfunction *h*, which form normal-mode solutions. Given an initial condition, we can

use the obtained normal-mode solutions to synthesize tsunami waveforms using equations (2.7) and (2.8).

2.1.3 Analytical Solutions of a 2D Rectangular Basin

If the area is a rectangle basin with uniform bathymetry, then an analytical solution of equation (2.5) exists. This is among the few cases that we can obtain an analytical solution for the normal mode solution. For a completely closed rectangular basin with length L in the *x* direction, width W in the *y* direction and uniform bathymetry *D* (Figure 2.1), we can write the equation (2.5) in the Cartesian coordinates:

$$D\left(\frac{\partial^2 h}{\partial x^2}+\frac{\partial^2 h}{\partial y^2}\right)=-\frac{\omega^2}{g}h \quad (2.10)$$

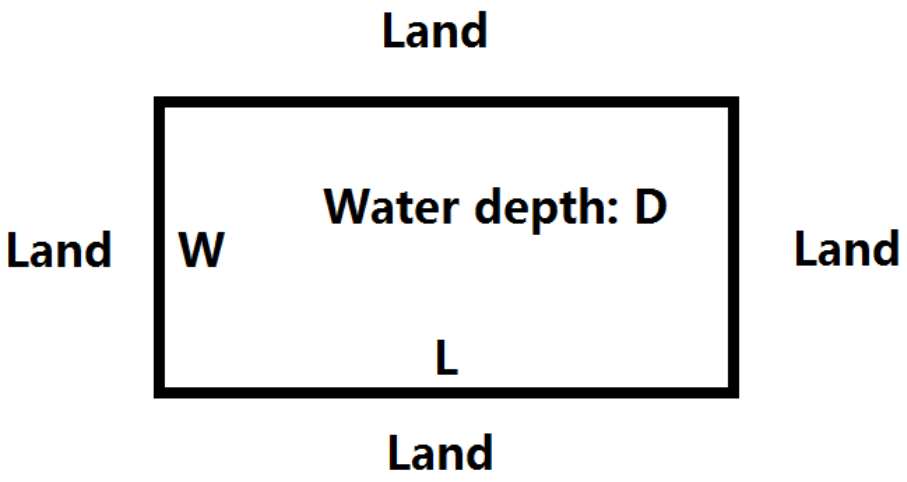

Figure 2.1. An illustration of the problem geometry: a rectangular basin with uniform water depth D, length L and width W, surrounded by land.

with land boundary conditions at all the four sides, that is:

$\frac{\partial h}{\partial x}=0$ at x=0 and x=L

$\frac{\partial h}{\partial y}=0$ at y=0 and y=W

Using separation of variables, set $h(x,y)= X(x)\cdot Y(y)$ and substitute it into (2.10), we then obtain:

$$\frac{1}{X}\frac{\partial^2 \mathrm{X}}{\partial x^2}+\frac{1}{Y}\frac{\partial^2 \mathrm{Y}}{\partial y^2}=-\frac{\omega^2}{gD} \quad (2.11)$$

Because the first term of the left side depends only on x, the second term of the left side depends only on y, and the right side is a constant, thus the first and second terms of the left side must be equal to two constants, respectively. Set the two constants to be $-\lambda_1$ and $-\lambda_2$, we get two equations:

$$\frac{\partial^2 X}{\partial x^2} + \lambda_1 X = 0 \quad (2.12a)$$

with boundary conditions $\frac{\partial X}{\partial x} = 0$ at x=0 and x=L

$$\frac{\partial^2 Y}{\partial y^2} + \lambda_2 Y = 0 \quad (2.12b)$$

with boundary conditions $\frac{\partial Y}{\partial y} = 0$ at y=0 and y=W

and $\lambda_1 + \lambda_2 = \frac{\omega^2}{gD}$

Solving (2.12a), we know that the solution has the form $X = cos\sqrt{\lambda_1}x$ (we discard the sine term because of the boundary condition $\frac{\partial X}{\partial x} = 0$ at *x*=0). Then using another boundary condition $\frac{\partial X}{\partial x} = 0$ at *x*=*L*, we get a relation:

$$\sqrt{\lambda_1}L = m\pi \quad \text{m} = 1,2,3 \ \ldots$$

Thus we obtain the solution $X = cos\frac{m\pi}{L}x$, *m*=1,2,3 … and $\lambda_1 = \left(\frac{m\pi}{L}\right)^2$

Similarly, solving (2.12b) yields $Y = cos\frac{n\pi}{W}y$, *n*=1,2,3 … and $\lambda_2 = \left(\frac{n\pi}{W}\right)^2$

Put all of them together, we get the solution of the (*m*, *n*) mode:

$$h_{mn}(x, y, t) = cos\frac{m\pi x}{L} cos\frac{n\pi y}{W} cos\omega_{mn} t \quad (2.13a)$$

$$\text{where } \omega_{mn} = \pi\sqrt{gD}\sqrt{\left(\frac{m}{L}\right)^2 + \left(\frac{n}{W}\right)^2} \quad (2.13b)$$

is the angular eigen-frequency.

In this case, we may also check the orthogonality of modes:

$$\int h_{ij}(\boldsymbol{x})h_{mn}(\boldsymbol{x})d\boldsymbol{x} = \int_0^L \cos\frac{i\pi x}{L}\cos\frac{m\pi x}{L}dx \int_0^W \cos\frac{i\pi y}{W}\cos\frac{n\pi y}{W}dy = \frac{LW}{4}\delta_{im}\delta_{jn}$$

Thus any solution $\eta(\mathrm{x},\mathrm{y},\mathrm{t})$ can be expressed as a mode superposition:

$$\eta(\mathrm{x},\mathrm{y},\mathrm{t}) = \sum_{m,n} C_{mn}\cos\frac{m\pi x}{L}\cos\frac{n\pi y}{W}\cos\omega_{mn}t$$

where C_{mn} is the excitation weight of each mode.

For rectangular basin with different boundary conditions (ex. node boundary instead of land boundary), the deduction is similar while some of the results may contains a sine function instead of a cosine function.

2.1.4 Analytical Solutions of a 1D case

For completeness, the analytical solution of equation (2.5) in 1D case with uniform bathymetry is also shown here. The equation is:

$$D\frac{\partial^2 h}{\partial x^2} = -\frac{\omega^2}{g}h$$

This is similar but far easier than the 2D case mentioned above. For one boundary condition $\frac{\partial \mathrm{X}}{\partial x} = 0$ at x=0 and x=L, the solution is:

$$h_m(\mathrm{x},\mathrm{t}) = \cos\frac{m\pi x}{L}\cos\omega_m t \quad (2.14a)$$

$$\text{where } \omega_m = \pi\sqrt{gD}\,\frac{m}{L} \quad (2.14b)$$

Other boundary conditions will yield similar results.

2.2 Numerical Calculation of NMM

2.2.1 Numerical Forms in the Cartesian Coordinates and the Construction of the Matrix Eigenvalue-Problem

Now we start to construct the matrix eigenvalue-problem equation (2.9) from equation (2.5) in the Cartesian coordinates following Loomis (1973).

In a staggered grid system in the Cartesian coordinates (Figure 2.2), the differential in the *x* direction in (2.7) can be discretized using central difference:

$$\frac{\partial}{\partial x}\left(D\frac{\partial h}{\partial x}\right) \rightarrow \frac{1}{\Delta x}\left\{Dx(i,j+1)[\frac{h(i,j+1)-h(i,j)}{\Delta x}] - Dx(i,j)[\frac{h(i,j)-h(i,j-1)}{\Delta x}]\right\}$$

And the similar for the y direction, thus we can get the numerical form of (2.7) in the Cartesian coordinates:

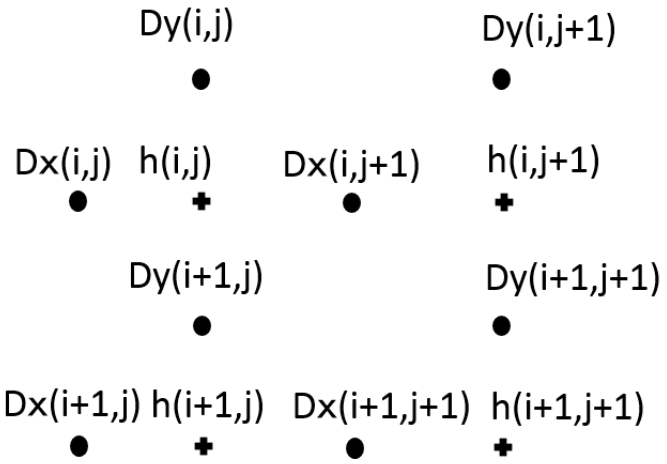

Figure 2.2. Staggered grid system in the Cartesian coordinates

$$\frac{\mathrm{Dx(i,j+1)}}{\Delta \mathrm{x}^2}\mathrm{h(i,j+1)} + \frac{\mathrm{Dx(i,j)}}{\Delta \mathrm{x}^2}\mathrm{h(i,j-1)} +$$

$$\frac{\mathrm{Dy(i+1,j)}}{\Delta \mathrm{y}^2}\mathrm{h(i+1,j)} + \frac{\mathrm{Dy(i,j)}}{\Delta \mathrm{y}^2}\mathrm{h(i-1,j)}$$

$$-\left[\frac{\mathrm{Dx(i,j+1)+Dx(i,j)}}{\Delta \mathrm{x}^2} + \frac{\mathrm{Dy(i+1,j)+Dy(i,j)}}{\Delta \mathrm{y}^2}\right]\mathrm{h(i,j)} = \lambda \mathrm{h(i,j)}$$

This is of the form:

$$a_{ij}(i,j+1)\mathrm{h(i,j+1)} + a_{ij}(i,j-1)\mathrm{h(i,j-1)}$$

$$+a_{ij}(i+1,j)\mathrm{h(i+1,j)} + a_{ij}(i-1,j)\mathrm{h(i-1,j)}$$

$$+a_{ij}(i,j)\mathrm{h(i,j)}=\lambda\mathrm{h(i,j)}$$

If we reorder double index ij as a single index I, and double index (i, j) as a single index J, that is to say $a_{ij}(i,j+1) \rightarrow a_{IJ}$, then we obtain: $a_{IJ}\mathrm{h}_I = \lambda\mathrm{h}_J$.

About the boundary conditions, node boundary h=0 is easy to achieve: just eliminate the corresponding element in vector h and matrix a. For land boundary $\frac{\partial h}{\partial n} = 0$, because the structure of $\nabla \cdot (D\nabla h)$, $\frac{\partial h}{\partial x}$ or $\frac{\partial h}{\partial y}$ is always coupled with *D*, so this kind of boundary can be achieved by setting *D* = 0.

Now we have already turned an eigenvalue problem of a differential equation into a matrix eigenvalue problem. That is, given a matrix a_{IJ}, find the set of pairs of eigenvalue λ_i and eigenvector $\mathbf{h}_i$. This may be solved by many excellent existing numerical methods. Noting that $a_{IJ} = a_{JI}$ so a_{IJ} is a symmetric matrix. As an example for I=ij and J=(i,j+1), we have:

$$a_{IJ} = a_{ij}(i,j+1) = \frac{\mathrm{Dx(i,j+1)}}{\Delta\mathrm{x}^2}$$

$$a_{JI} = a_{ij+1}(i,j) = \frac{\mathrm{Dx(i,j+1)}}{\Delta\mathrm{x}^2}$$

The symmetry promises all the eigenvalue and eigenvector are of real numbers, which makes the numerical problem easier to solve. Another important property of a_{IJ} is that it is a very sparse matrix, which contains only 5 elements per row. And dimension of a_{IJ} is n times n, n is the total number of ocean grid. This means if we double the number of grids in both x and y direction, the dimension of the new matrix will be 16 times of the original one, instead of 4 times. Here lies the difficulty of a high-resolution calculation.

2.2.2 Numerical Forms in the Spherical Coordinates and an Experiential Normalization Method

In the previous research of Loomis (1973) and Satake and Shimazaki (1987), they used Cartesian coordinates when discretizing equation (1). However, for an area like the Sea of Japan, which spans more than 10° of latitude from north to south, a spherical coordinate system is more suitable. In this study, spherical coordinates are used in the numerical scheme, so equation (2.5) becomes:

$$\frac{1}{R^2 \sin\theta}\frac{\partial}{\partial\theta}\left(D \sin\theta \frac{\partial h}{\partial\theta}\right) + \frac{1}{R^2 \sin^2\theta}\frac{\partial}{\partial\varphi}\left(D \frac{\partial h}{\partial\varphi}\right) = \lambda h$$

where θ is the co-latitude and φ is longitude. In the staggered grid system used in this study (Figure 2.3), this equation has the discrete form of:

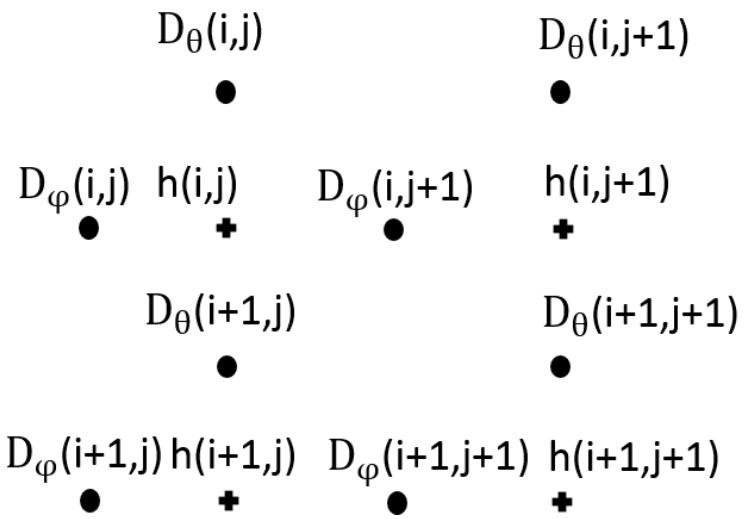

Figure 2.3 Staggered grid system in the spherical coordinates

$$\frac{D_\varphi(i,j+1)}{s(i)^2 R^2 \Delta\varphi^2} h(i,j+1) + \frac{D_\varphi(i,j)}{s(i)^2 R^2 \Delta\varphi^2} h(i,j-1)$$

$$+ \frac{s'(i+1) D_\theta(i+1,j)}{s(i) R^2 \Delta\theta^2} h(i+1,j) + \frac{s'(i) D_\theta(i,j)}{s(i) R^2 \Delta\theta^2} h(i-1,j)$$

$$- \left[\frac{D_\varphi(i,j+1) + D_\varphi(i,j)}{s(i)^2 R^2 \Delta\varphi^2} + \frac{s'(i+1) D_\theta(i+1,j) + s'(i) D_\theta(i,j)}{s(i) R^2 \Delta\theta^2}\right] h(i,j)$$

$$= \lambda h(i,j) \qquad (2.15)$$

where D_φ and D_θ represent the water depth at the grid point in the θ and φ directions, respectively, since in a staggered grid system, two depth grid systems are required; s represents the value of $sin\theta$ at the corresponding D_φ (or h); and s' represents the value of $sin\theta$ at the corresponding D_θ. Notice that equation (2.15) has the form of equation (2.9).

Using the original orthogonality of normal modes equation (2.6), all the integration has to deal with the $d\boldsymbol{x}$ part, which is varying with the latitude in the spherical coordinate system. For simplicity, I first assume that $d\boldsymbol{x}$ is not changing, so that an experiential normalization equation (2.16) as in the Cartesian coordinates can be used:

$$\sum_{i,j} h_l(i,j)h_m(i,j) = \delta_{lm} \quad (2.16)$$

The assumption generally holds since the change of $d\boldsymbol{x}$ from north to south in the Sea of Japan is relatively small. The results in Section 3 and 4 will be based on this experiential normalization equation. While the exact normalization and its application will be provided and discussed in Section 5. And in Section 5 it is shown that waveforms derived from these two normalization equations have significant differences only before the onset.

Using equation (2.16), mode superposition equation then remains the same form as (2.7):

$$\eta(\boldsymbol{x},t) = \sum_l C_l h_l(\boldsymbol{x}) cos\omega_l t \quad (2.17)$$

while the mode excitation weight C_l now has a new form:

$$C_l = \sum \eta_0(\boldsymbol{x}) h_l(\boldsymbol{x}) \quad (2.18)$$

where the summation is taken over the whole ocean grids.

As shown, if we use Cartesian coordinates, the constructed matrix a_{ij} is symmetric (Loomis, 1973), which mathematically guarantees all the eigenvalues and the eigenfunctions to be real numbers. Currently matrix a_{ij} is not symmetric due to the differentiation along the θ direction. In this case, the problem has to be solved by allowing the eigenvalues and eigenfunctions to be complex numbers. Although this makes the calculation more difficult, the eigenvalue solver introduced in Section 2.2.3 can handle this problem. An important physical insight into our eigenvalue problem is that, because there is no energy flux into or out of the region of interest, all the

eigenvalues and eigenfunctions should be real numbers. However, since we now solve the asymmetric eigenvalue problem, the results may contain imaginary parts due to computational instability. Whether our numerical calculation can overcome this kind of potential instability remains a challenge. Another way to overcome the asymmetry is to construct a symmetric eigenvalue-problem, which will be demonstrated in Section 5.1.

2.2.3 Acceleration of the Numerical Calculation

Previous studies (Loomis, 1973; Satake & Shimazaki, 1987) employed an inefficient method to solve the matrix eigenvalue-problem, which made it impossible to deal with the problem in a large dimension. To obtain high-resolution normal-mode solutions in a large area like the Sea of Japan, we introduce the following method:

(1) Because the structure of matrix a_{ij} is sparse, with at most five elements in a row, we can store the matrix linearly by ignoring all the zero elements; storing diagonal, subdiagonal, and superdiagonal entries p_i, q_i, and r_i, respectively, in three arrays; and storing the value of the other two entries x_i and y_i and their corresponding indices in another array. A brief illustration of the structure of a_{ij} is shown in equation (2.19), where the locations of x_i and y_i are arbitrary.

$$\begin{bmatrix} p_1 & r_2 & & & x_1 & y_1 & & \\ q_2 & p_2 & r_3 & x_2 & & & y_2 & \\ & q_3 & \ddots & \ddots & & x_3 & & y_3 \\ & & \ddots & \ddots & \ddots & & & \\ & & & \ddots & \ddots & \ddots & & \\ & & & & \ddots & \ddots & \ddots & \\ & & & & & \ddots & \ddots & r_n \\ & x_n & & & y_n & & q_n & p_n \end{bmatrix} \tag{2.19}$$

(2) We implement a matrix-vector multiplication that requires $O(n)$ instead of the usual $O(n^2)$ computation time, where n is the dimension of the matrix. That is,

$$w_i = a_{ij}v_j = q_i v_{i-1} + p_i v_i + r_{i+1} v_{i+1} + x_i v_{index(x_i)} + y_i v_{index(y_i)}$$

where the *index* function indicates the index of the element x_i or y_i in the storage array.

(3) We use an implicitly restarted Arnoldi method (IRAM) provided by Arpack library (Lehoucq et al., 1996), an iteration method that fully utilizes a fast matrix-vector

multiplication process. This method also provides solvers for asymmetric problems. Therefore, it is suitable for our calculation, since we are using the spherical coordinates.

With the improvements mentioned above, we make it possible to calculate high-resolution normal-mode solutions for the Sea of Japan, which is the key to synthesizing tsunami waveforms using NMM

2.2.4 Test of Rectangular Basin in the Cartesian Coordinates

Before we calculate the normal mode of a real area, it is a good idea to first do some test to verify the numerical method developed above with analytical solutions. Here I choose a completely closed rectangle basin with a uniform depth and computed the eigenvalue $\lambda = -\frac{\omega^2}{g}$ and compare them with the analytical solution (2.13b).

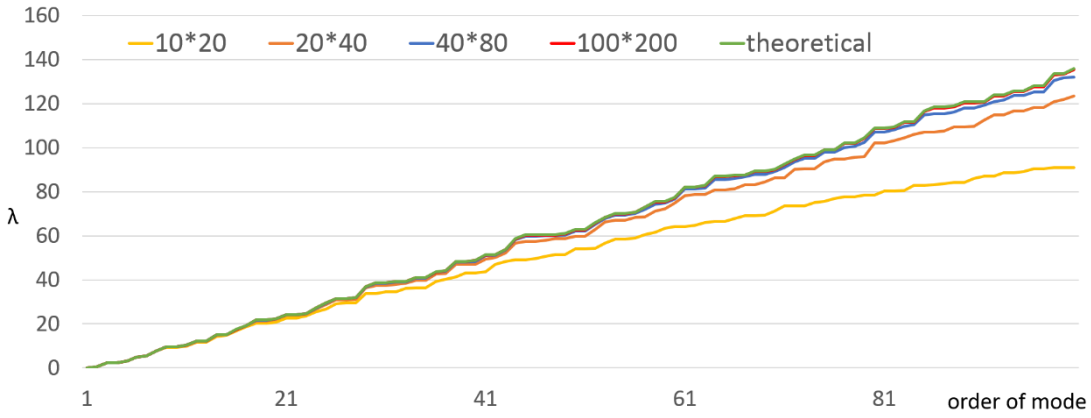

Figure 2.4 Comparison of calculated λ with theoretical value in a closed rectangle basin. Different numbers of grids are used for the same area.

For the same area, I try to calculate using different numbers of grids. From Figure 2.4 we can see that, the numerical result trend to converge to the theoretical one, when we use finer grids. This infers us that the result of numerical calculation is reliable when we have finer grids. Therefore, it is very important to conduct normal mode calculation with higher resolution bathymetry data.

I also plot the calculation time to obtain 100 mode in Figure 2.5. We can then understand how difficult it would be to obtain a high-resolution normal mode solution in the past. After these efforts made in Section 2.2.3, I finally find a reasonable way to handle a large dimension NMM problem.

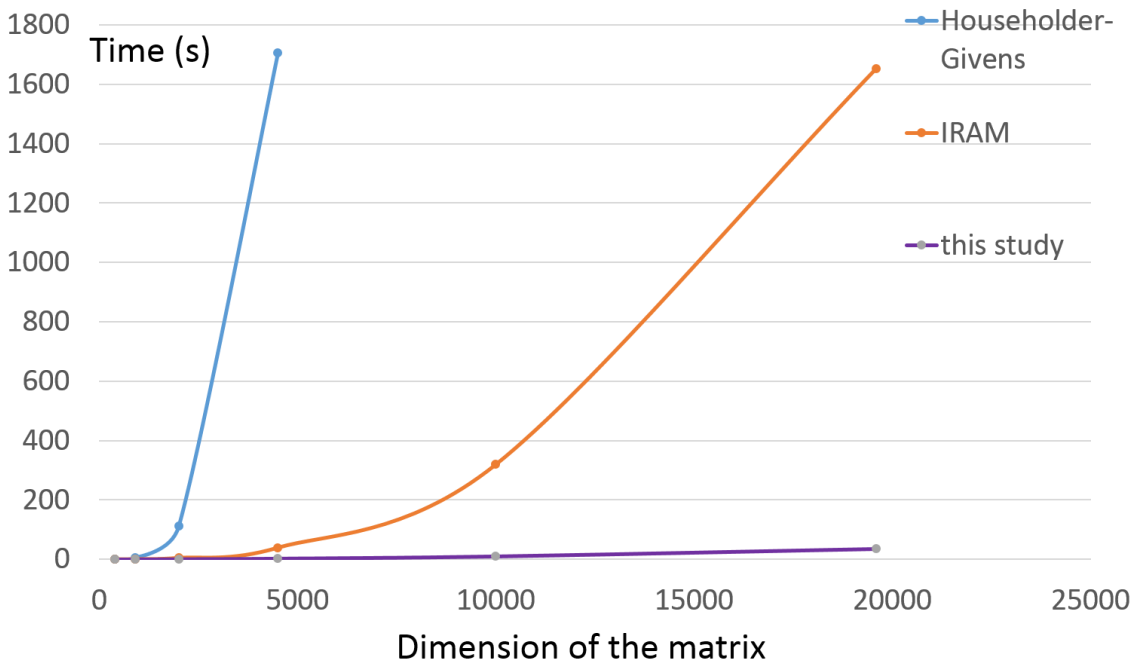

Figure 2.5 Comparison of time needed to get 100 modes in single precision using symmetry solver by 1. Householder-Givens method used in Loomis (1973) 2. IRAM directly 3. IRAM with improvements mentioned in this study.

2.2.5 Parallelization with MPI

The numerical calculation of the matrix eigenvalue-problem is extremely time consuming, even with the mentioned improvement in Section 2.2.3. To further accelerate the calculation, parallelization is needed. Fortunately, there is a parallel library of IRAM called Parpack (Maschhof and Sorensen, 1996). The library offers two choices of message passing, one is MPI (Message Passing Interface) and another is BLACS (Basic Linear Algebra Communication Subprograms). Here I chose to use the MPI implementation. Most things are similar to the serial version when using the serial IRAM, except that:

(1) The originally linearly stored matrix is divided into several parts according to the number of cores used in the calculation. Each part is now stored and processed (as much as possible) in the corresponding core (Figure 2.6).

(2) The matrix vector multiplication required by IRAM modified to a parallel version. Of course now message passing is required.

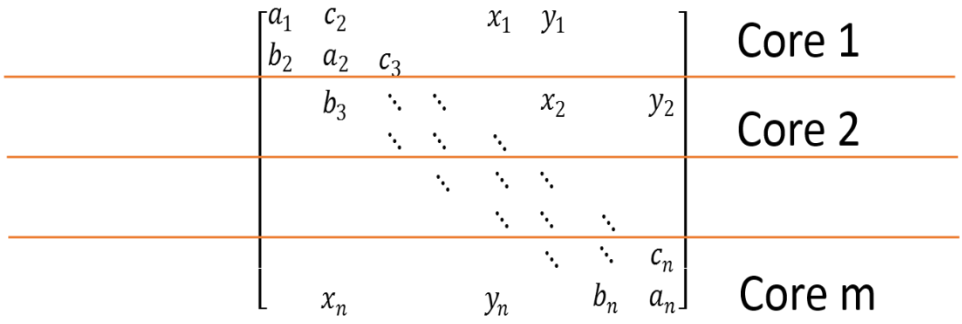

Figure 2.6. Illustration of the matrix distributed in each core

Then with the parallel version of the code, test calculations are made. These calculations aim to calculate the first 100th, 200th, 400th and 800th modes of the 2-arc-min Sea of Japan, with different number of cores used. Table 2.1 shows the calculation time for each case and Table 2.2 shows the actual efficiency of one core for each case. (Single core efficiency is set to one).

Table 2.1 Calculation time of 100, 200, 400 and 800 leading modes of the 2-arc-min Sea of Japan, using 1, 8, 32, 64, 432 cores on EIC computer system, respectively. The unit is second.

Modes / Cores	100	200	400	800
1	2910	5080	14277	81613
8	558	1101	3170	21431
32	255	384	1240	9971
64	207	292	921	8737
432	62	101	510	6642

Table 2.2 Actual efficiency of one core for each case (Single core efficiency is set to one)

Modes / Cores	100	200	400	800
1	1	1	1	1
8	0.65	0.58	0.56	0.48
32	0.35	0.41	0.35	0.26
64	0.21	0.27	0.24	0.15
432	0.11	0.12	0.065	0.028

From these results, first we see reduction of calculation time when using more cores. Second, we find that the calculation efficiency decreases when the number of cores

increases, as well as the dimension of the problem increases. This is firstly due to that the communication part of the current program is not optimized. Another reason is related to the nature of the parallel IRAM used because it is not fully parallelized: there is a key step to generate the Arnoldi factorization

$$\boldsymbol{AV_b = V_b H_b + f_b e_b^T}$$

where $\boldsymbol{A}$, with dimension n x n, is the matrix in equation (2.9), $\boldsymbol{V_b}$, with dimension n x b, is the set of Arnoldi vectors, (b is the number of modes to calculate), $\boldsymbol{f_b}$ is the residual vector and $\boldsymbol{H_b}$ is the b x b projection matrix. The problem is that $\boldsymbol{H_b}$ is replicated on every processor (so does operations on $\boldsymbol{H_b}$). So when b is larger, the scalability becomes worse. In contrast, when n increases (ex. when grid size decreases) while keep b the same, the paralleled calculation time increases only linearly, which is a good point.

Besides, there is another parameter *k*. In order to obtain *b* eigenvectors, the IRAM actually keeps iteration on *k* vectors and k is larger than *b*. Therefore, the selection of *k* also affects the calculation time. The following Table 2.3 shows the calculation of *b*=1000 modes using 432 cores with different *k*. Since larger *k* means less vector-matrix multiplication while more work at Arnoldi factorization, a small *k* results faster calculation. Here, the proper choice of *k* makes the calculation of 1000 modes even faster than that of 800 modes in Table 2.1.

Table 2.3 calculation time of 1000 modes of the 2 arc-min Sea of Japan using different number of iterating vectors *k*.

k	time/s
1500	4095
2000	14872
4000	30470

As a conclusion, the parallelization with MPI even without optimization enables a moderate acceleration, if combined with a proper choose of *k* and with moderate number of cores. And parallelization is especially suitable when the dimension n of the problem is increased while the required number of modes is kept. Actually in the next Section we will see that when the grid size is decreased, similar mode order has still similar frequency.

2.3 Modal Solutions of the Sea of Japan

In this study, we focus on tsunamis in the Sea of Japan, which are suitable for the new NMM. The Sea of Japan is far larger than a bay but still of a moderate size. Thus, our new calculation can show the improvement clearly while still being computationally manageable. Also, we can compare the result with that obtained from Satake and Shimazaki (1988) to evaluate the development of the method. They used a grid size of around 10 arc-min and obtained only 100 modes, which made it impossible to synthesize tsunami waveforms from the obtained mode solutions.

To calculate the normal-mode solutions for an ocean basin, the only input data needed is the bathymetry. We use the 30 arc-sec General Bathymetric Chart of the Oceans (Intergovernmental Oceanographic Commission, International Hydrographic Organization, and British Oceanographic Data Centre, 2003) and resampled it to generate 2 arc-min grids as the input bathymetry, which reduced the eigenvalue-problem dimension. Another resampled 1 arc-min grids are also constructed as an input for the parallel computation. The boundary contained four straits, as shown in Figure 2.7a. For strait 1 (Tatar Strait), we set it to be a land–ocean boundary because the water depth there is less than 10 m. For the other three straits, we set them to be open ocean boundaries, or nodes.

The normal-mode solutions for the Sea of Japan are calculated using the bathymetry input. The dimension *n* of the matrix a_{ij} was 95,148 for the 2-arc-min grids case (as a contrast, the matrix in Satake and Shimazaki (1988) is of dimension 2521). In total, 6,000 modes are obtained with periods down to about 8.3 min, much shorter than 50 min, the shortest period obtained by Satake and Shimazaki (1988). The calculation time of 6,000 modes is about 15 days on an ordinary desktop computer. All the obtained eigenvalues and eigenfunctions have a zero imaginary part. Figure 2.8 shows the frequency distribution of the 6,000 modes, where modes are ordered starting from longer period. From the distribution, we can observe a decrease in the slope as the order of the mode increases. This means that the number of modes in a given frequency band becomes larger as the order increases.

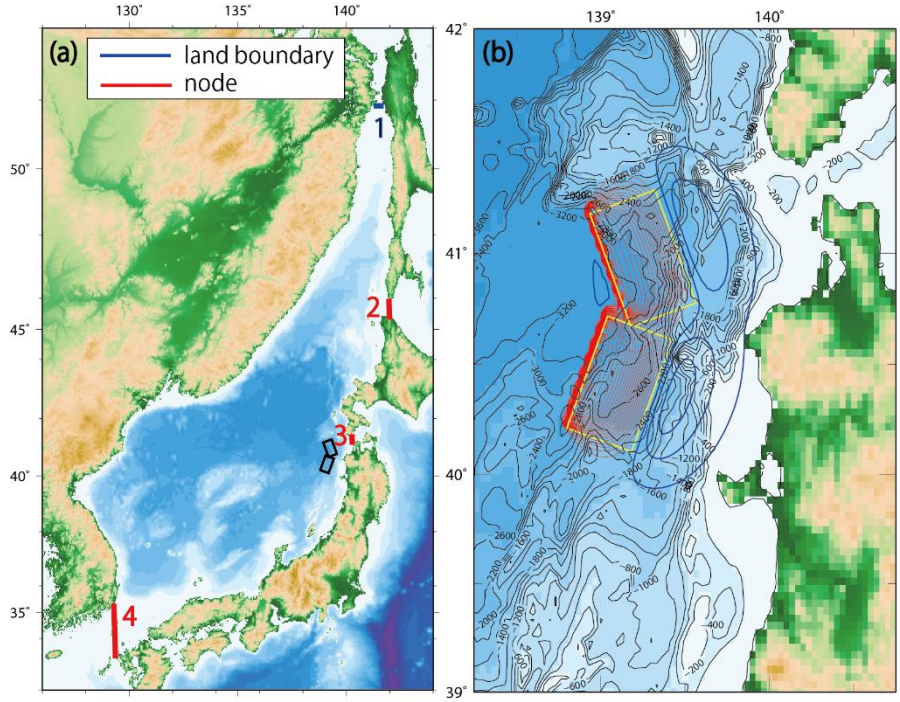

Figure 2.7. (a) Bathymetry of the Sea of Japan with domain boundaries marked as lines. The faults of the 1983 Sea of Japan earthquake proposed by Satake (1985) are shown by yellow rectangles. (b) Enlarged map near the faults of the 1983 Sea of Japan earthquake. The red and blue contours are the uplift and subsidence, respectively, calculated by Okada's method (1985), with an interval of 0.1 m.

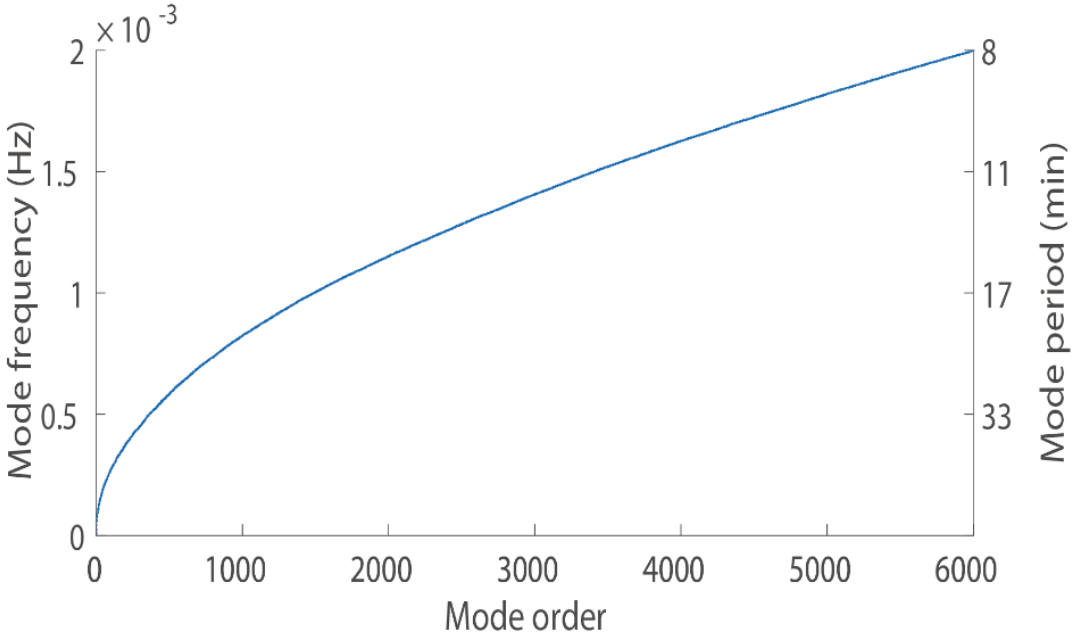

Figure 2.8. Frequency distribution of the 6,000 modes obtained by NMM, where modes are ordered starting from longer period.

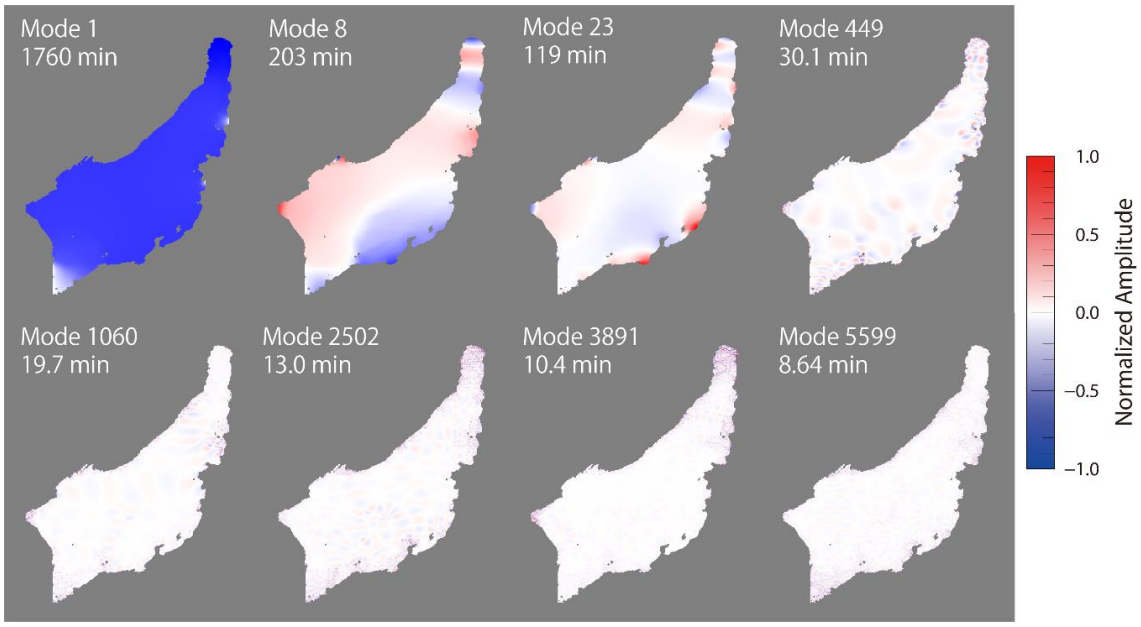

Figure 2.9. Oscillation patterns (eigenfunctions) for selected modes. Red and blue mean opposite oscillations, while white indicates a node (zero amplitude).

Figure 2.9 shows the oscillation pattern (eigenfunction) for some selected modes. The amplitude is normalized by the largest amplitude of that mode to show the pattern more clearly. The polarity is not important as long as it is coupled with excitation weights defined in equation (2.7), because a mode $h_i(\boldsymbol{x})$ is mathematically equivalent to a mode $-h_i(\boldsymbol{x})$ in equations (2.5)–(2.8). We can see several white areas between the boundaries of red and blue areas. These are nodes of the mode, where the oscillation amplitude is zero. As the mode order increases, more nodes appear, which means the wavelength is becoming shorter. Because of the mode normalization, as the mode affects a larger area, its overall amplitude decreases. As a reference, see the 1D case (Figure 2.14).

For the parallel computation of 1 arc-min grids, the dimension *n* of the matrix a_{ij} is 380,662, which is already larger than a 2 arc-min Mediterranean Sea. In total, we have obtained 3,000 modes with periods down to about 11.5 min. The calculation time is about 77 hours on EIC computer system using 64 cores. Figure 2.10 shows the mode order versus mode frequency for the obtained 1 arc-min grids solution and the 2 arc-min ones. Similar mode order has close mode frequency for the same region. This is an important property since we can estimate the mode order obtained from finer grids based on coarser grids. In the following part, otherwise specified, I use the 2 arc-min solution since it covers higher frequency.

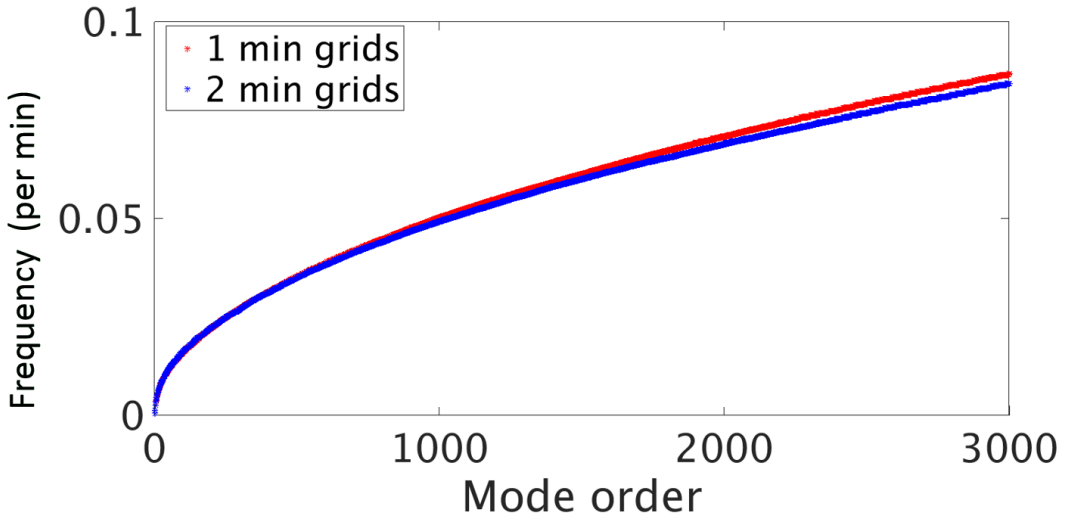

Figure 2.10. Comparision of the relation between mode order and mode frequency for the obtained 1 arc-min grids solution and the 2 arc-min solution of the Sea of Japan

After obtained modal solutions, modal analysis is usually conducted. Here I rather not conduct a traditional modal analysis, but want to point out an interesting issue usually ignored by many modal analysis researches. Figure 2.11 shows an enlarged view of mode 8 in Figure 2.9 with bathymetry counters. Many modal analysis papers such as Bellotti et al., (2012b), Cortés et al. (2017) stated that mode pattern is related to either bathymetry or the shape of the costal line. From Figure 2.11 however, we may find that none of these are true (at least impossible to observe), if the oscillation is global. Actually this is rather obvious when refer to a 2D rectangular case with uniform water depth, where the only thing can be observed is that the nodal lines are parallel/perpendicular to the sides and other conclusions are very hard even for this simple case. Therefore, in this thesis I rather do not conduct traditional modal analysis of the whole Sea of Japan. While in Section 4, source characterization using NMM is presented. This can be considered as a novel modal analysis which cannot be conducted before, since none of the researches were able to include the source fault into the interested region, nor did they deal with higher modes in a large region.

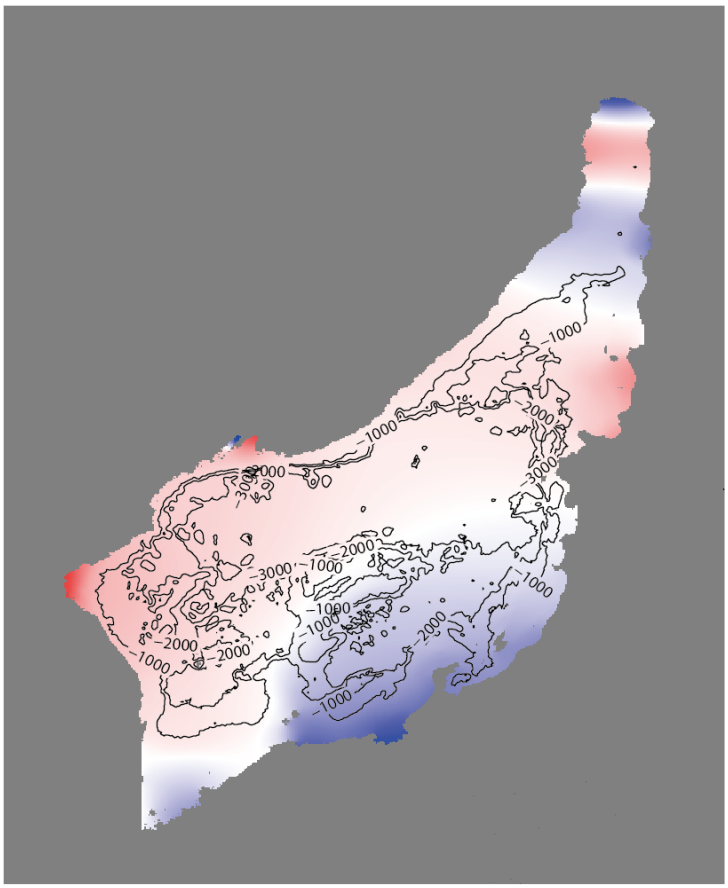

Figure 2.11. An enlarged view of mode 8, with bathymetry contours.

2.4 A Relationship between Mode Order and Mode Frequency

For a given calculation area, we may have a target frequency upper limit, that is, we may want to cover a frequency band up to a high frequency limit. However, when we do normal mode calculation of a given area, only after we obtain the modal solutions do we first know the frequency band coverage. For a small region like Tokyo bay, this is fine because we can easily get several hundreds of modes, which covers the energy band of the tsunami signal (if the grid size is not too fine). But for a large dimension target like the Sea of Japan, this is not desirable. Since we cannot know the frequency band our modal solution can cover until we get a modal solution, while to get the modal solution itself takes rather long time. Therefore, if we can establish a relationship between the mode order and the mode frequency, we can have many insights before starting the numerical calculation. This relationship may seem hard to establish, yet we have got some hints from the known analytical and numerical modal solutions.

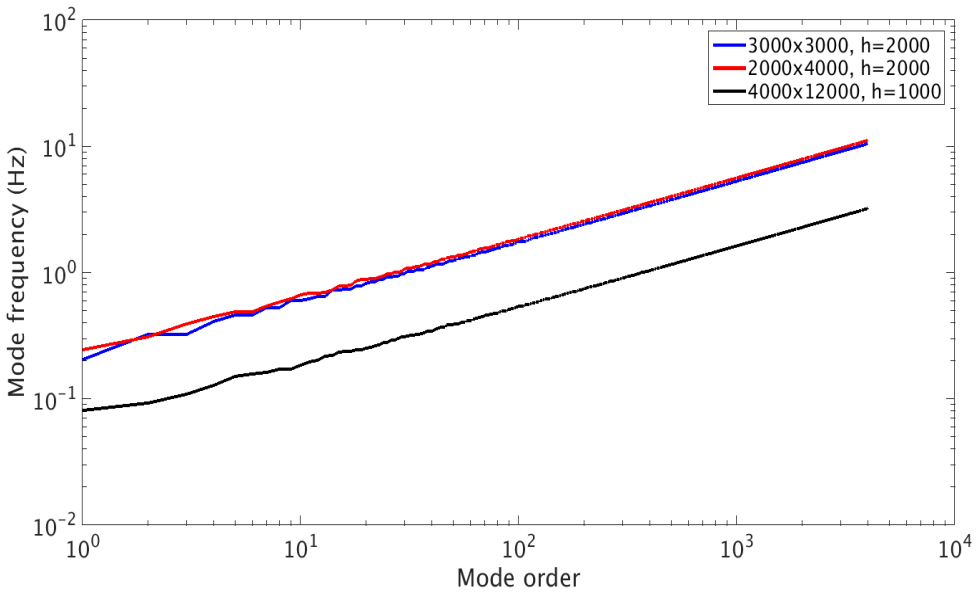

Figure 2.12. Analytical relationship between mode order and mode frequency for 3 ideal rectangular basins. Blue, red and black line represent the results from 3 rectangular basin with 3000m x 3000m, 2000m x 4000m, 4000m x 12000m in size, and of 2000m, 2000m, 1000m water depth, respectively.

Figure 2.12 shows the relationship between mode order and mode frequency for 3 analytical cases. These are solutions from 3 ideal rectangular totally closed basin with uniform water depth. The size and water depth of each basin are 3,000m x 3,000m and 2,000m, 2,000m x 4,000m and 2,000m, and 4,000m x 12,000m and 1000m, respectively. In this logarithm scale plot, we find that these are three "straight" lines (if we only focus on the higher order) parallel with each other, although the intercept may be different. This plot gives hint that the relationship may be similar for the problem with the same dimension.

Then in Figure 2.13, the relationship between the mode order and the mode frequency in 3 cases are plotted: the Sea of Japan numerical case, the 1D analytical case and the 2D rectangular numerical case. In this logarithm scale plot, we find that for higher modes, the slope of the 1D case is 1, and the slope of the 2D rectangular case as well as the Sea of Japan case is 1/2, they are parallel.

For these analytical cases, this can be proven. In 1D case, recall the relationship equation (2.14b), mode frequency f is proportional to ω_m, which is proportional to the mode order m.

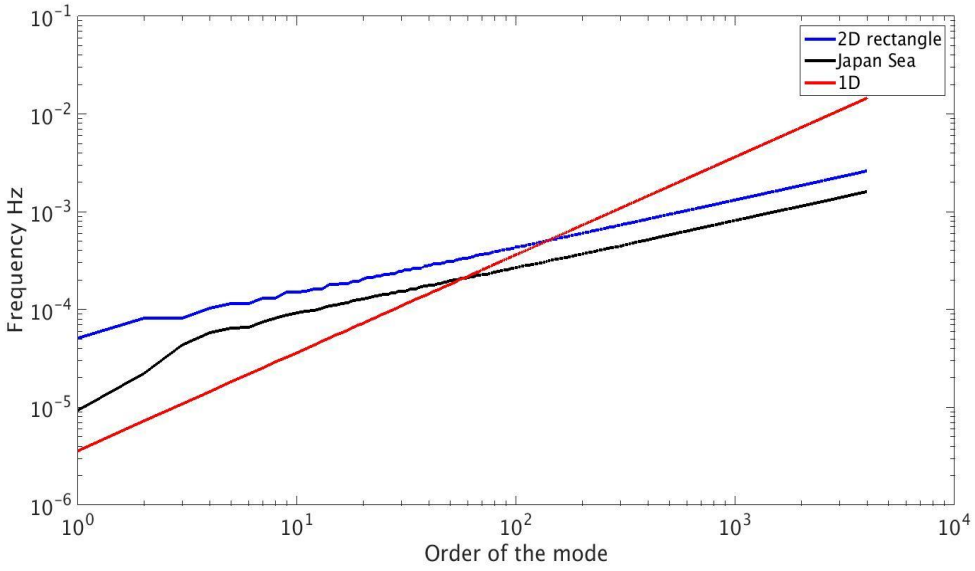

Figure 2.13. Relationship between mode order and mode frequency for 1D and 2D ideal cases as well as the numerical Sea of Japan case.

In 2D case, recall equation (2.13b), mode frequency f is proportional to $\sqrt{\left(\frac{m}{L}\right)^2+\left(\frac{n}{W}\right)^2}$, while mode order is not obvious here. By its definition, mode order is determined if we can sort the $\left(\frac{m}{L}\right)^2+\left(\frac{n}{W}\right)^2$ array and therefore a function of *m* and *n*. One thing is clear that the point (*m*, *n*) has larger value of $\left(\frac{m}{L}\right)^2+\left(\frac{n}{W}\right)^2$ than all points with smaller *m* and *n*. So the mode order is roughly proportional to *mn*. Therefore, *f* is proportional to the square root of the mode order, if *L* and *W* are of similar order.

From the two analytical cases, we may conjecture that in a logarithmic scale, the mode frequency is proportional to the mode order, with a slope determined by the dimension of the problem, that is the reciprocal of the dimension:

$$\log(\mathrm{f}) = \log(\frac{o}{\mathrm{dimension}} + b)$$

Here *o* is the order of the mode and *b* is the intercept.

Therefore, in the Sea of Japan case, we may also get:

$$f = bo^{1/2} \quad (2.20)$$

Using the data from mode order 2,000 to mode order 4000, we get $b = 2.5672\text{x}10^{-5}$. So we obtained a relationship between the order of the mode and the frequency of the mode in the Sea of Japan:

$$f = 2.5672 \times 10^{-5} o^{1/2} \quad (2.21)$$

Using this formula to predict the frequency of mode order 6,000 yields 503s, and the numerical solution yields 501s, which means the deduced formula is fairly good approximation. Also notice that equation (2.21) predicts that the 15,000th mode has period of 314s, while the calculated result in Section 5.2 is 303s. We can say that extrapolation using only 2,000 modes yields a reasonable prediction.

Combined with the parallel code developed in this study, the following procedure is advised when dealing with new calculation: We may first use the parallel computing to get the leading say 1,000 or 2,000 modes, which can be done in a rather short time. Then using these obtained modes, we may estimate a similar formula as equation (2.21) and then we can have ideas about the relationship between the mode order and the mode frequency before a further detailed calculation.

2.5 An Automatic Mode Grouping Method

Different from the traditional modal analysis, to better understand the properties of their 100 calculated modes, Satake and Shimazaki (1988) roughly grouped them as two kinds, the whole Sea of Japan modes and regional modes, according to the area that each mode affects. Here, with far more calculated modes and a higher spatial resolution, I have adopted criteria to divide these modes into three groups with the help of a statistical quantity: basin-wide modes, regional modes, and local modes. The basin-wide mode affects almost the whole Sea of Japan. The regional mode affects a large region but is not basin-wide. The local mode only has high energy in very local structures, such as a very small bay.

An appropriate statistical quantity was needed to group the modes. Variance—$Var(X) = E[(X - \mu)^2]$, where μ is the expected value of the data set X and E is the mathematical expectation function—is used to describe the deviation of data from their average level and seemed to be a good candidate. However, because the difference of

variance is less pronounced even in two extreme cases (Figures 2.14a and 2.14d), it fails to clearly discern the mode types. In this study, we adopt the statistical quantity kurtosis (Kurt), whose definition is $Kurt(X) = \frac{\mu_4}{\sigma^2} = \frac{E[(X-\mu)^4]}{(E[(X-\mu)^2])^2}$. Higher kurtosis means a larger variance but infrequent extreme deviations.

To facilitate better visualization of the difference, 1D examples are shown in Figure 2.14. Here we use a similar number of 1D grid points as the 2D Sea of Japan case as in Section 2.3. We consider both panels (a) and (b) as basin-wide modes, (c) as a regional mode, and (d) as a local mode. From this figure, we can also see the advantage of using kurtosis instead of variance, whose difference is less than 1 digit between the 2 extreme cases (panels a and d). It is necessary to note that the cross-section of a 2D case is not identical to the corresponding 1D case because of the additional dimension.

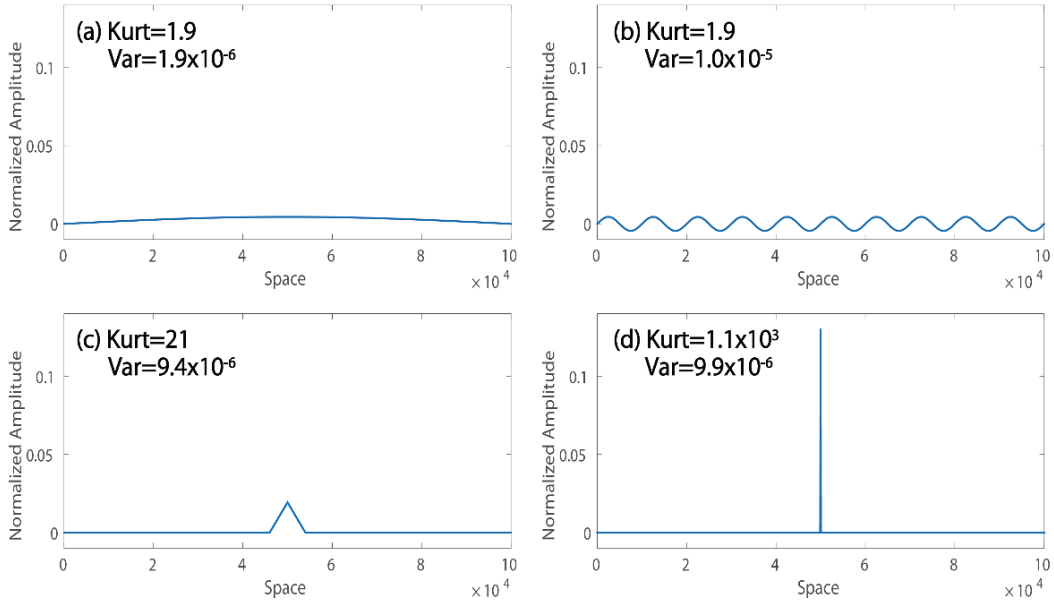

Figure 2.14. Four normalized 1D modes and their corresponding kurtoses and variances. Panels (a) and (b) are basin-wide modes, while (c) and (d) are regional and local modes, respectively.

Then I apply this grouping method to the modal solution of the Sea of Japan to form three mode groups. By visual inspections and trial and error, we defined modes with a kurtosis value smaller than 35 as basin-wide modes, those between 35 and 350 as regional modes, and those larger than 350 as local modes. Using these thresholds, 622 basin-wide, 4,953 regional, and 425 local modes are obtained.

To illustrate the characteristics of each group, I select five representative modes to show the continuum from a “pure” basin-wide mode to a “pure” local mode (Figure 2.15).

The oscillation pattern for the first mode (No. 8, Kurt=4) is basin-wide. Near the boundary between the basin-wide and regional modes (Kurt=39), we see partial basin-wide oscillation, and there are also some regional structures emerging near the coast. Then at Kurt=145, oscillations are confined to only part of the basin. Near the boundary between the regional and local modes (Kurt=344), the pattern is vague but more localized (concentrated near the south-west corner in this case). For the local mode (Kurt=4,802), all oscillations are limited to a very small area (at the south-west corner here).

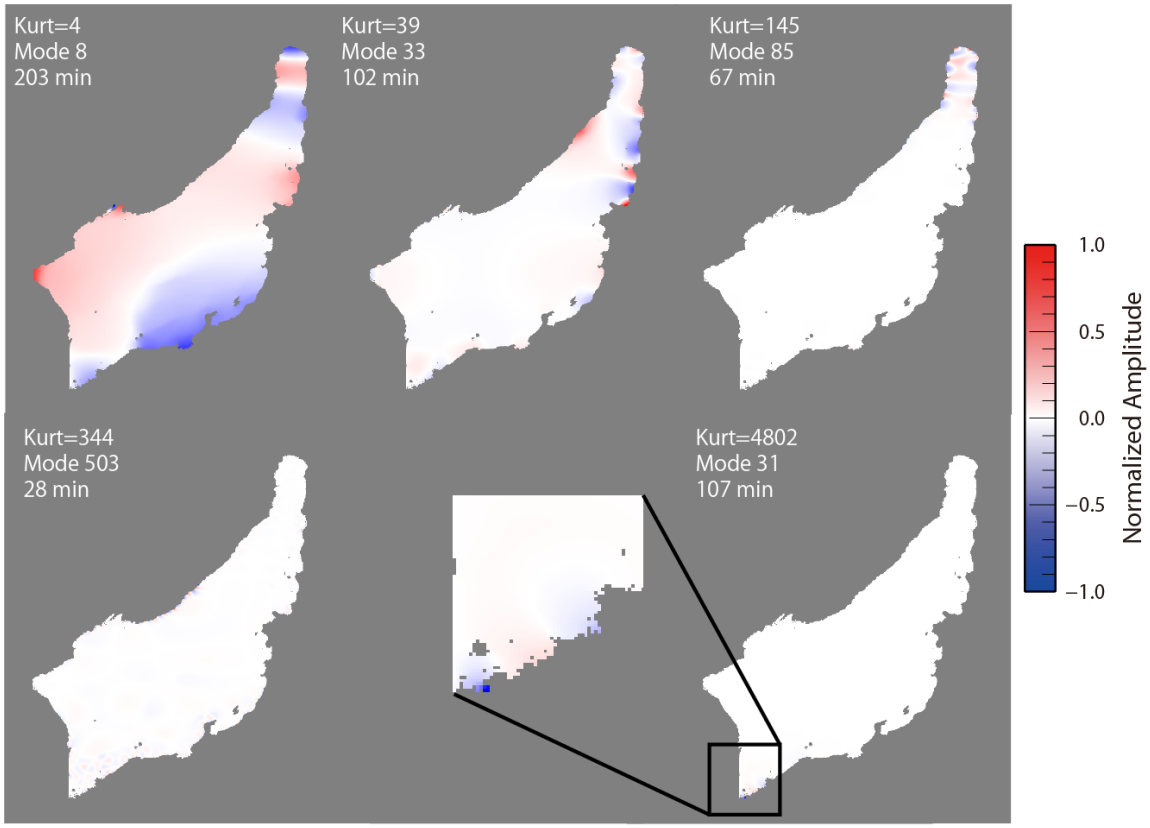

Figure 2.15. Five modes demonstrating the difference between basin-wide modes (Kurt=4), regional modes (Kurt=145), and local modes (Kurt=4,802); two transitional modes (Kurt=39 and 344) are also shown.

3 TSUNAMI EXCITATION SYNTHETIZED BY MODE SUPERPOSITION AND ITS PROPERTIES

3.1 The 1983 Sea of Japan Earthquake

After obtaining the high-resolution normal-mode solutions for the Sea of Japan, we proceed to synthesize tsunami waveforms using the NMM.

In this study, we choose the May 26, 1983, Mw 7.7 Sea of Japan earthquake, which is among the largest instrumentally recorded events inside the Sea of Japan, and it generated a destructive tsunami. The tsunami affected a wide area along the coast of Japan, as well as the Korean Peninsula and Russia. This earthquake led to 104 fatalities, with 100 of them caused by the tsunami. According to Watanabe (1998), the highest tsunami wave was about 14 m at Minehama village, which is located in the northern part of Akita Prefecture in Japan.

Fault model from Satake (1985) is used, which contains two rectangular subfaults with slip amounts of 5 m (northern part) and 4 m (southern part). The static ocean bottom displacement is calculated using Okada's method (1985), and the initial sea surface displacement is assumed to be the same as the seafloor displacement (Figure 2.7).

Notice that the dominant tsunami period T by the fault can be estimated by:

$$T = \frac{\lambda}{v} = \frac{2L}{\sqrt{gD}}$$

where g is the gravitational acceleration, D is the water depth in the source region, and L is the width or length of the fault. There is a factor two in the numerator because a full waveform consists of both uplifted and subsided parts, as shown in Figure 2.7b. The water depth in the source region is around 2,500 m, and the shorter edge of the fault has a length of 40 km. Therefore, the lower boundary of the dominant period is about 8.5 min, which is covered by our modal solution.

3.2 Simulation Results by NMM and Comparisons with FDM

With the initial sea surface displacement and the normal-mode solutions, we have calculated the weight of each mode using equation (2.18). With these weights, the tsunami waveforms at any position could be calculated using equation (2.17). Here, a cosine taper is used for the weights of the 1,000 highest-order modes to smooth the result.

Figure 3.1 compares the waveforms calculated by NMM and FDM (Satake, 1995), both based on the same 2-arc-min grids, at three tide gauge stations, Iwanai, Saigo, and Kutsugata. Comparison of the two simulation methods shows that they are almost identical at Iwanai, where the amplitude of the later phases is different, while the shape of the waves still has a good match at Kutsugata and the later phases are totally different at Saigo. For Kutsugata and Saigo, the reasons for such differences may be mainly due to the frequency (period) of computed tsunami waves. At Iwanai, the FDM waveform is almost in the frequency range covered by the mode solution, which is down to 8.3 min. At Saigo, the FDM waveform contains high-frequency oscillations that are out of the range of calculated modes. While at Kutsugata, the frequency coverage is probably not the reason as we will see in Section 5.3. The discrepancy is more likely due either to that Kutsugata is located near the node boundary (since the node boundary is very different from the usual open ocean boundary) or to that Kutsugata is located where the bathymetry changes rather dramatically. The observed tsunami waveforms (Japan Meteorological Agency, 1984) are also shown as a reference. We suspect that the

difference between the simulations and observations is due to the rather coarse grid size (2-arc-min) of the bathymetry data.

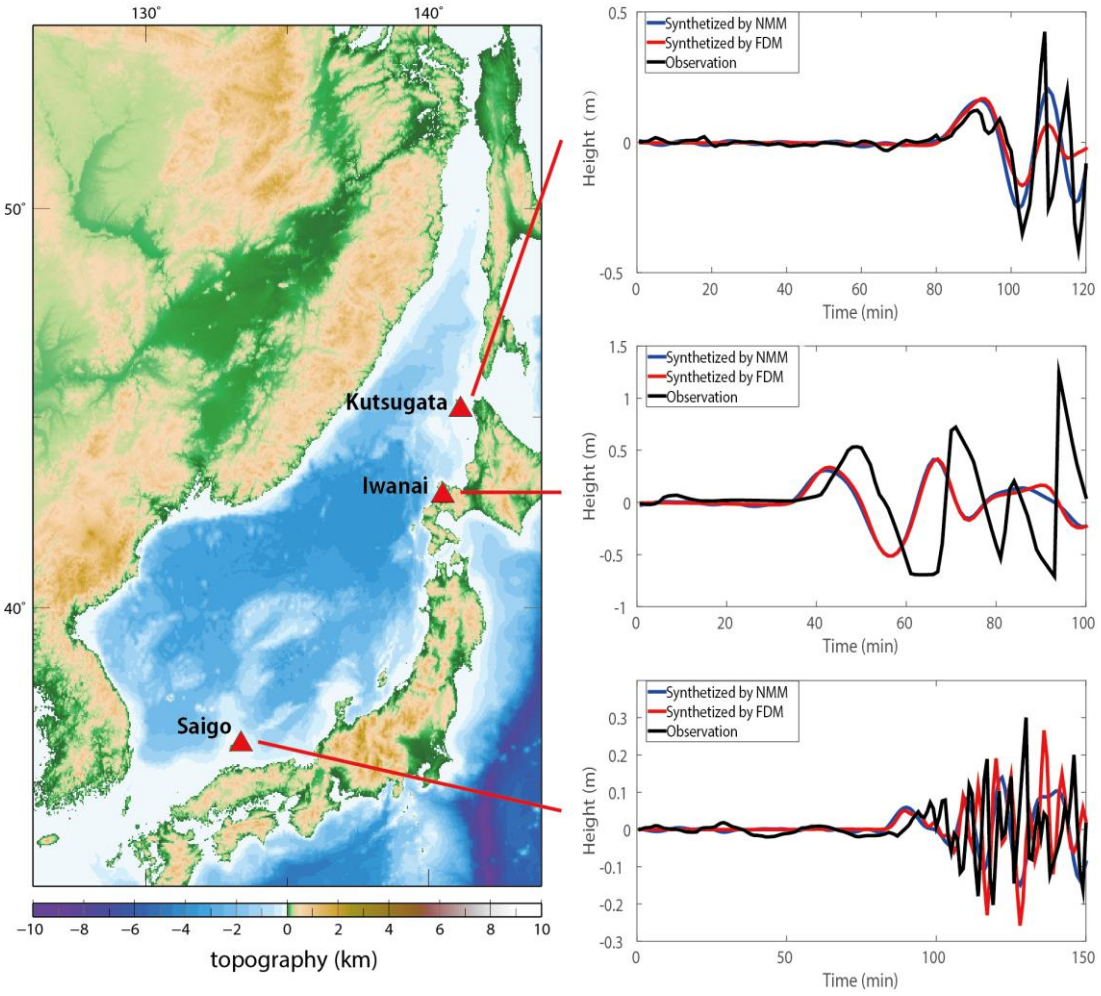

Figure 3.1. Synthesized tsunami waveforms using NMM at Iwanai, Saigo, and Kutsugata (blue lines). As a reference, the synthesized tsunami waveforms using FDM (red lines) and actual observations (black lines) are also plotted.

3.3 Modal Superposition Process

Figure 3.2 shows an example of the mode superposition process for the Iwanai waveforms shown in Figure 3.1. Waveforms synthesized by superposition of the first 1,000, 2,000 and 6,000 modes, which covers periods down to 20 min, 15 min, and 8 min, respectively, are shown. Here the cosine taper applied in Section 3.2 was not used. The same FDM result as in Figure 3.1 is also plotted as a reference.

This figure illustrates the mechanism behind the mode superposition. It also shows the importance of acquiring more modes. Most notable is that at the second positive wave

(after 60 min), the NMM result is closer to that of FDM when we add more modes for superposition.

It is also counterintuitive but an expected feature that, before the first wave comes, mode superposition using a large enough number of modes will result in nearly zero amplitude.

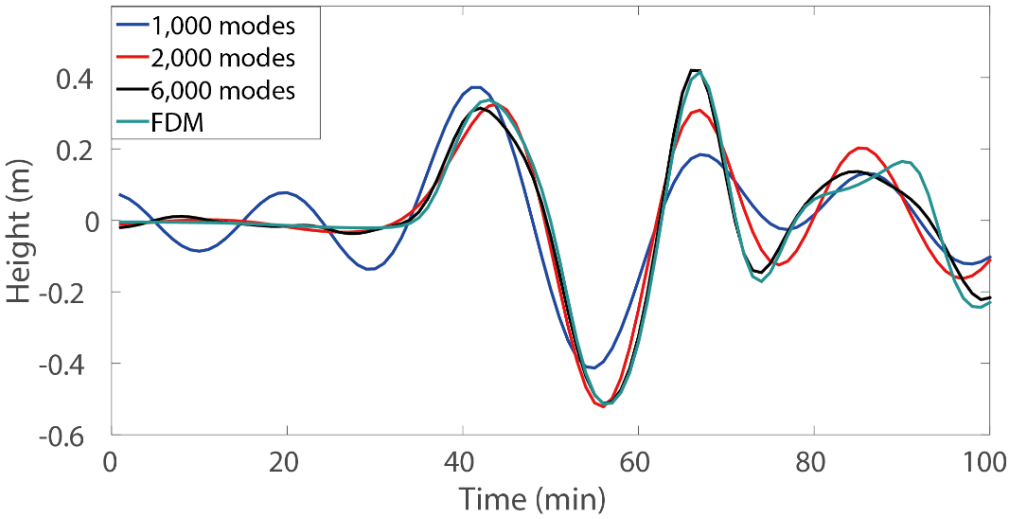

Figure 3.2. Mode superposition process for tsunami waveforms of the 1983 Sea of Japan earthquake at Iwanai station. Blue, red, and black lines are the waveforms synthesized using the first 1,000, 2,000, and 6,000 modes, respectively. Green line is the synthesized waveform using the FDM.

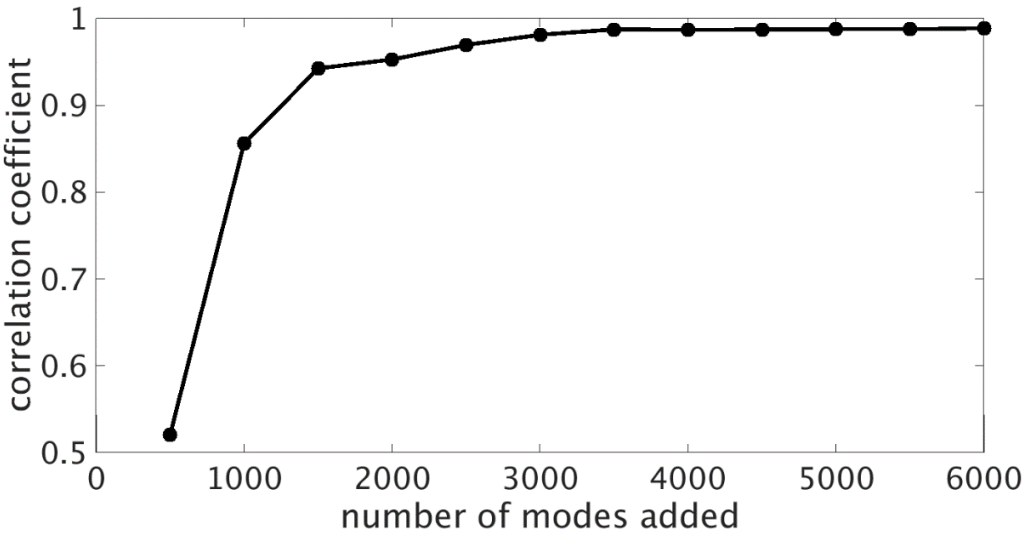

Figure 3.3. Correlation coefficient between FDM simulated waveform and NMM simulated waveforms from superposition of different numbers of mode, at Iwanai.

Figure 3.3 shows the correlation coefficient of waveforms at Iwanai, simulated by FDM and NMM mode superposition. The result is similar as in Figure 3.2: when more modes are added, the match becomes better.

3.4 A Way to Estimate the Required Mode Number

In Section 3.2 and 3.3 we have shown the NMM performance from the view of time domain. Here, a view from the frequency domain is presented. Figure 3.4 shows the power spectrum of the observed tsunami data as in Figure 3.1. The frequency band covered by the 2-arc-min NMM solution of the Sea of Japan is also added. Then the goodness of NMM waveform synthetization is clear: For Iwanai, the strong energy peaks are all covered by the NMM frequency band, therefore the waveform synthesized at Iwanai presented the best match. For Kutsugata, one of the strongest energy peaks lies within the frequency band coverage boundary, therefore the frequency coverage is probably enough. For Saigo, the main peak is not covered by the NMM solution, therefore a poor synthesized waveform is not strange.

Then with the relationship between the mode order and the mode frequency obtained in Section 2.4, we now have a way to estimate the required mode number to reproduce the tsunami waveforms at a given place. The general process is like the following:

1. Calculate the power spectrum of the tsunami waveforms at a given place either using some historical data or using the background noises.
2. From the energy peaks or minor peaks, decide an upper limit of frequency that the calculation may want to cover.
3. Using the relationship between the mode order and the mode frequency equation (2.20), estimate the required mode order.

Now we follow this procedure to estimate the required mode number for Saigo. (while for Iwanai, the match is already fairly good).

For Saigo, the major peak is located at around 400s, that is equivalent to 9,500 modes. While minor peaks are located at around 330s, that is equivalent to 14,000 modes. Therefore, to have the synthesized waveform to match roughly, 9,500 modes are need while in order to have a fine reproduction of the waveforms, 14,000 modes are needed.

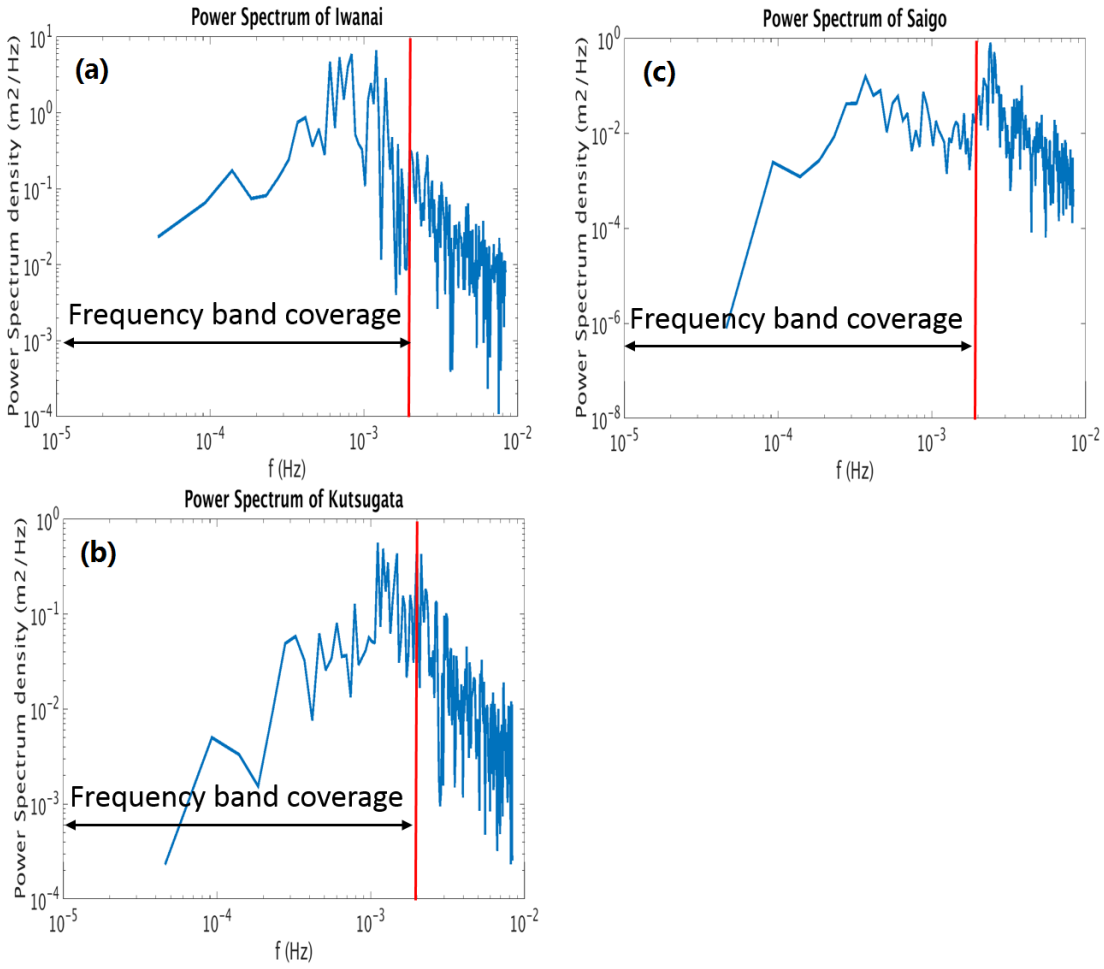

Figure 3.4. Power spectrum of the observed waveforms at three stations.

3.5 Calculation Time of NMM Simulation and an Improvement

While the NMM method is thought to have the advantage of being able to conduct waveform simulation really fast, it is necessary to measure the actual time cost and compare it to other methods like FDM (Satake, 1995). Table 3.1 shows the tsunami simulation time using NMM and FDM in the Sea of Japan in 2-arc-min grids and 1-arc-min grids. For the NMM, number of modes used are 6,000 for 2-arc-min grids and 3,000 for 1-arc-min grids. For FDM, the numerical computations are both made for 180 minutes of tsunami propagation, and time step *dt* are 2s for 2-arc-min grids and 1s for 1-arc-min grids. We can see small advantage in 2-arc-min grids case while around a 10-time acceleration in 1-arc-min grids. Although the simulation time of FDM itself is not long because the Sea of Japan region is not that large.

When grids size is halved, the time consumption of NMM is theoretically around 4 times longer because now there are four times more grids take part in mode superposition. While for FDM, the time consumption becomes 8 times because in addition to the increased ocean grids, *dt* need also be halved.

Table 3.1 Comparison of tsunami waveform simulation calculation time by FDM and NMM

	2 min grids	1 min grids
NMM	8.9s	24s
FDM	14s	219s

Although this measurement shows some advantage of NMM, it seems not satisfying. In order to accelerate the NMM waveform simulation, one easy idea raised from improving the time consuming part. When doing NMM waveform simulation, the mode solutions need to be read into memory from the disk first. This I/O (input and output) process take a large portion of NMM calculation time and can be reduced by using faster storage devices like solid state disk.

Here we would rather propose a major improvement that accelerate the NMM waveform simulation by several orders. According to equation (2.8), the excitation weight is calculated based on the initial condition over the whole ocean grids. For the usual earthquake faults, static displacement tends to zero when the distance from the fault increases. Therefore, it is reasonable to assume that the fault displacement is zero outside some region. This region is rather larger than the fault region, but far smaller than the whole ocean region.

In the case of the Sea of Japan, for the Sea of Japan earthquake, a 3°x 3°area (Figure 3.5) is enough to reproduce the same simulation result as using the whole ocean grids. Instead of the former 8.9s, now the overall simulation time is around 0.2s. The improvement is roughly proportional to the ratio between the ocean grids taken part in the calculation before and after. With this improvement, even in the Sea of Japan NMM proves its great waveform simulation speed against FDM.

Another good property of the improvement is that now, instead of the whole ocean grids, the calculation time is proportional to the size of the selected interested area around the source. This size is rather determined by the magnitude of the earthquake and have an upper limit. Therefore, even when dealing with a larger area than the Sea of

Japan, the NMM simulation time will remain the similar. Now NMM simulation time is affected only by the grid size, but not by the total size of the calculation area.

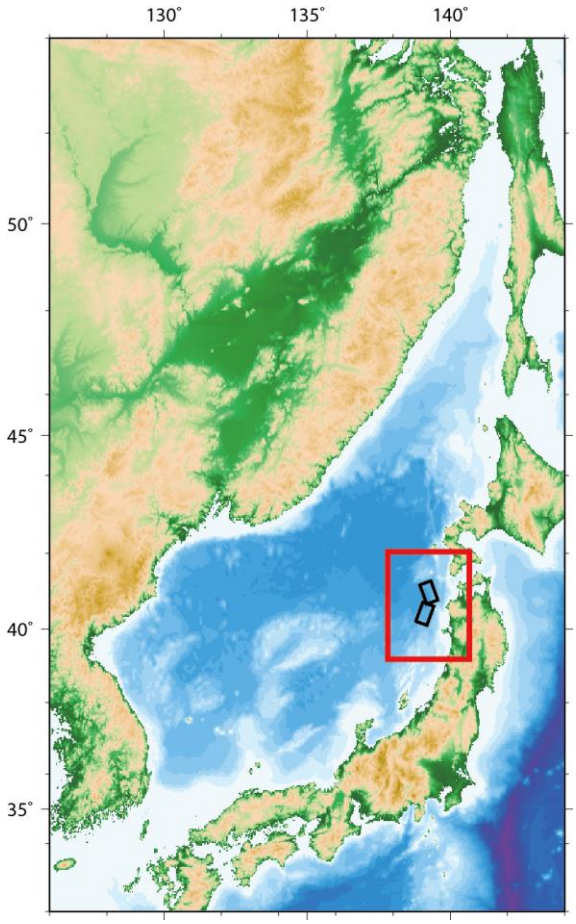

Figure 3.5. Reduced 3°x 3° calculation area in red when conducting NMM waveform simulations

4 SOURCE CHARACTERIZATION IN THE SEA OF JAPAN USING NMM

4.1 Hazard in Sea of Japan and MLIT Faults

A Japanese government committee that investigated large earthquakes in the Sea of Japan proposed parameters for 60 faults along the eastern margin of the Sea of Japan (locations of these fault can be found in Figure 4.1), and these were published by the Ministry of Land, Infrastructure, Transport and Tourism (MLIT, 2014). Hereafter, we refer to these as the MLIT fault models. The purpose of the MLIT report was to provide realistic fault models for tsunami hazard assessments by local (prefectural) governments on the coast of the Sea of Japan. Using submarine seismic reflection data, they located active faults and established their length and strike angles. The assigned dip angles were mostly 90º, 45º, 60º, or 30º. The fault widths were estimated from the thickness of the seismogenic zone (either 15 or 18 km) and the dip angle. The slip angles were assigned from the tectonic stress field; most faults in the northern areas are reverse faults, whereas those in western areas are strike-slip faults. The slip amounts were determined

using the scaling relation of Irikura and Miyake (2001) considering the variance of the parameters. Detailed MLIT fault parameters can be found in Appendix A.

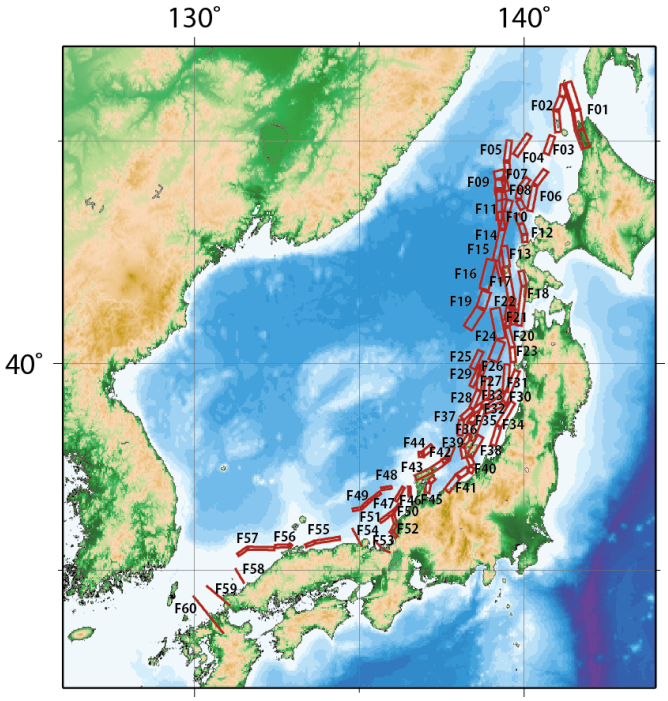

Figure 4.1. 60 potential submarine faults proposed by MLIT.

4.2 General Factors that Affect the Amplitude of Average Excitation Weight

The excitation weight for each mode is calculated for the 60 MLIT fault models (Appendix B). Figures 4.2a and 4.2b show weights for several faults with different magnitudes located near shore and off the coast of the Tohoku region. When we compare faults at similar locations (faults 1 and 4 or faults 2 and 3), the faults with larger magnitude (Mw 7.8) had larger excitation weights than those with smaller magnitudes (Mw 7.3–7.4). Thus, the first observation is that weights are larger for faults with larger magnitudes. We then compare the faults with similar magnitudes but different locations (faults 1 and 2 or faults 3 and 4) and noted that faults near shore with shallower water depths had larger weights than those at offshore locations with deeper water depths. Similar conclusions could be drawn from other comparisons, as shown in Figure 4.2b. From these comparisons, we conclude that when the source has a larger magnitude, or is located at a shallower water depth, the overall excitation weights are larger.

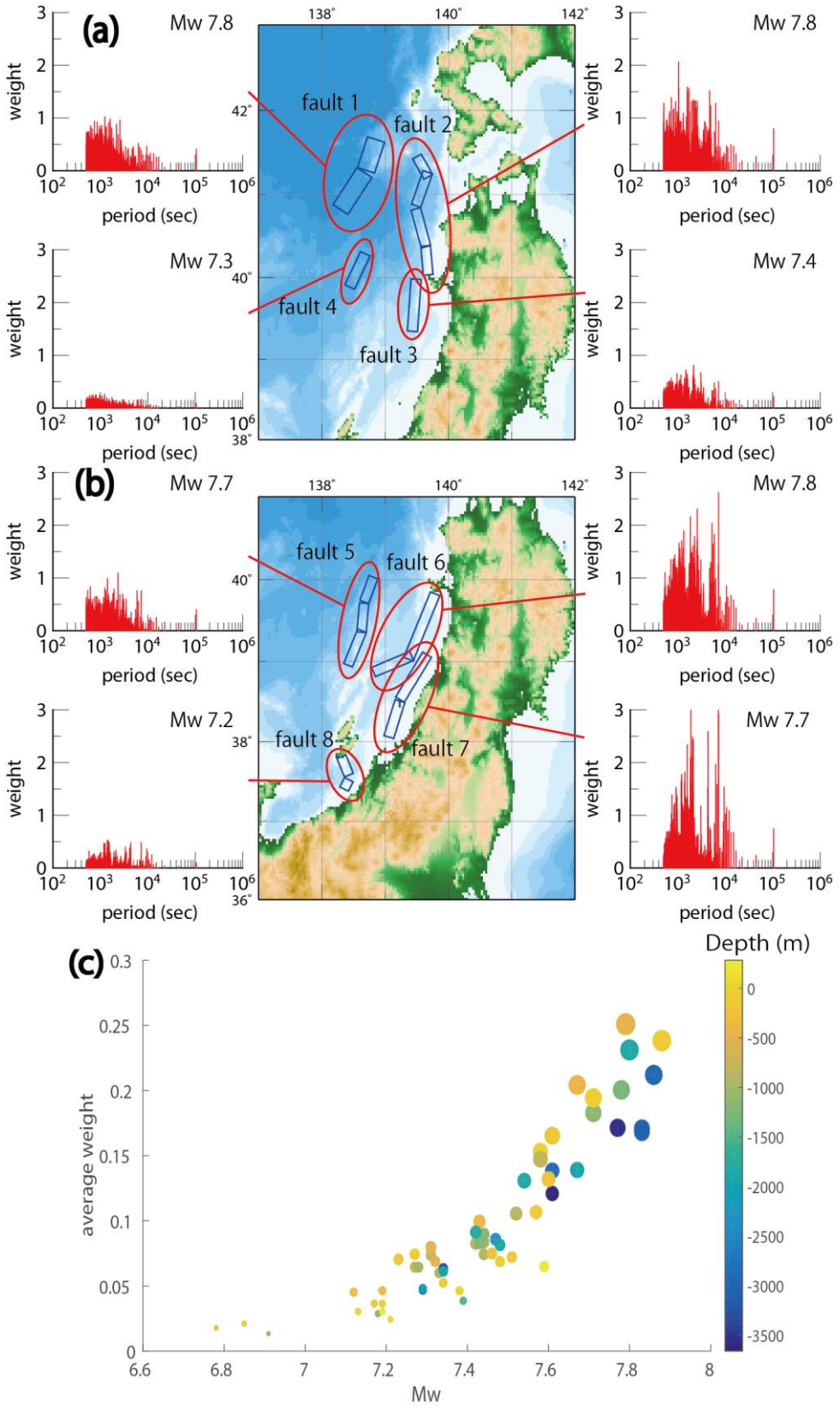

Figure 4.2. (a) and (b) Selected average excitation weights of events. (c) Average excitation weight of each event versus its magnitude. Different colors indicate the depth of the source. The size of the circle is proportional to its magnitude.

To confirm the above conclusions for the entire the Sea of Japan, we calculate and plot the average excitation weight of each fault versus its magnitude and water depth (Figure 4.2c). First, from the relation between the magnitude and excitation weight, it is quite clear that the average weight increased as the magnitude increased. Next, we observe the vertical variation for the same magnitude, and we find that, for the events with similar magnitudes, the upper positions are usually occupied by the events with shallower water depths. To further understand these relationships, we need to consider the contribution from different mode groups.

4.3 Excitation Weight for Different Groups of Mode and the Importance of Regional Modes

We examine the contribution of basin-wide, regional, and local modes to the excitation for each fault. Because the number of modes for each type is different (622, 4,953, and 425, respectively), we compute the average of the top 425 highest-order modes in each type (Figure 4.3a).

We find that among these three types of modes, the weight for the regional modes increased fastest as the magnitude of the source increased. This indicates that the contributions of regional modes become more significant for faults with larger magnitudes. To further examine the contribution of regional modes to faults, we separate the 60 faults by their water depth (shallower or deeper than 1,000 m) and plot them in Figure 4.3b. This figure shows that the weight for sources located at shallower water depths increase faster as the magnitude of the source increased. This indicates that the contribution of regional modes is more significant for faults at shallower water depths. This is probably due to the fact the regional modes have larger amplitudes at shallower water depths.

I then examine the amplitude distributions for some of the regional modes. Figure 4.4 shows the five regional modes with the largest average excitation weights for the 60 faults. These regional modes all have a larger amplitude at some shallower parts. Many other regional modes also have strong oscillation amplitude at these locations, where the usual submarine faults are located. Thus, these regional modes are more sensitive to potential submarine faults, especially shallow faults.

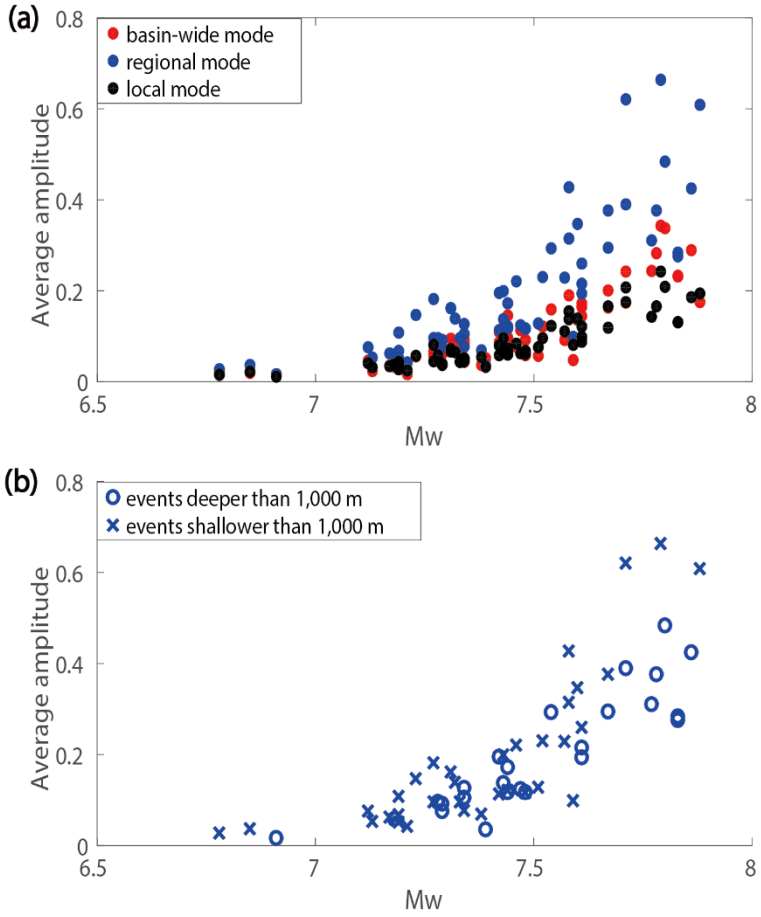

Figure 4.3. (a) Average excitation amplitude against source magnitude for three different mode groups. (b) Average excitation amplitude of regional modes against source magnitude, grouped by water depth at the source.

To have a clear view of the waveform contributions from local modes, Figure 4.5 shows the mode superposition at Iwanai with and without the local modes. We can see that, although the local modes do have some nonnegligible contributions, they neither have large contribution, nor do they shape the waveforms.

To confirm that regional modes have more influences than the other two groups, I plot in Figure 4.6 the relationship between a mode's kurtosis, which determines its group (remember that basin-wide modes are defined as Kurt < 35), regional ones as 35 < Kurt < 350, and local ones as Kurt > 350), and the average excitation weight of this mode over 60 MLIT submarine faults. The figure shows that, with very few exceptions, regional modes (these around the peak) do have the largest energy contributions. The envelope (red arrows) demonstrates the properties of modes' energy. For basin-wide modes, energy is distributed through the whole Sea of Japan, therefore they yield

similar weights. Then for regional modes, some have most of the energy at the MLIT sources region, thus with larger weights (the ascending upper arrow), while some have much energy off the MLIT sources region, thus with smaller weights (the descending bottom arrow). Finally for local modes, because their energy are confined in a region that is much smaller than the MLIT sources' region, they only yield smaller weights (both the descending upper and bottom arrows).

Figure 4.4. Five regional modes with the largest average excitation weights for the 60 faults. The locations of large amplitudes (indicated by red ellipses) correspond to the locations of the 60 faults.

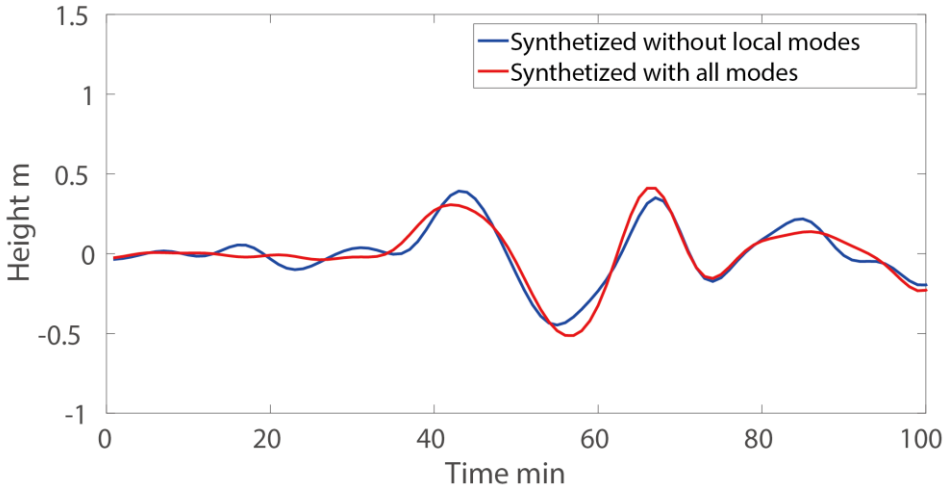

Figure 4.5 NMM simulated waveforms at Iwanai with and without local modes.

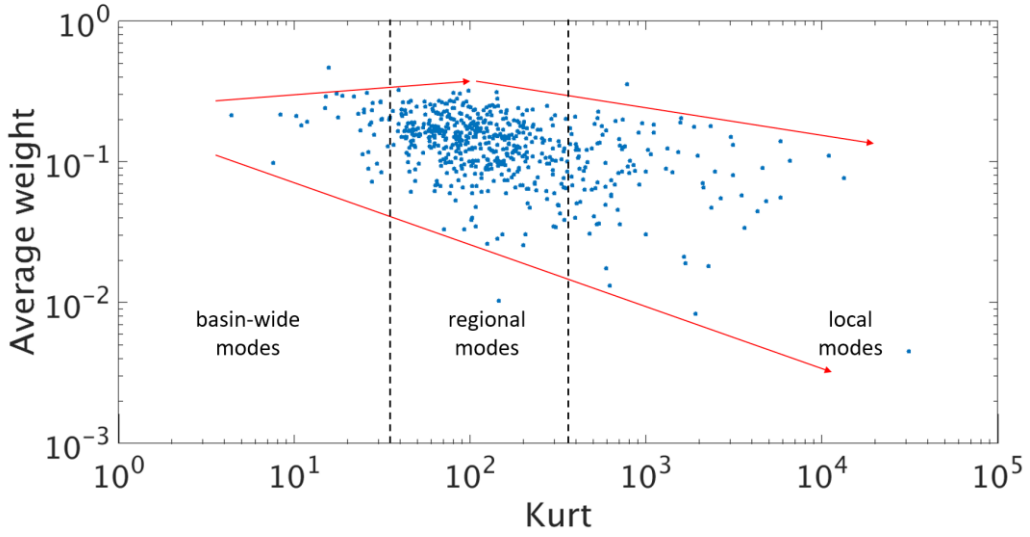

Figure 4.6 Relationship between a mode's kurtosis, which determines its group, and the average excitation weight of this mode over 60 MLIT submarine faults. Red arrows form an envelope of most of the points and show the ascending and descending trends when modes turn from a basin-wide one, through a regional one and finally to a local one.

Therefore, in contrast to regional modes, whose energy is distributed much more efficiently to affect a large coastal area, basin-wide modes have their energy distributed through the whole Sea of Japan, and local modes distribute their energy in a very small area. A summary is shown in Table 4.1.

Table 4.1 Contributions from each group of modes

	Basin-wide modes	Regional modes	Local modes
Excitation weight C_i	moderate	moderate - large	small
Energy distribution $h_i(\boldsymbol{x})$	Very wide	A large coastal area	Very confined
Contribution	Low	High	Low

For these reasons, more attention and further detailed studies are needed for these regional modes.

5 A SYMMETRIC CONSTRUCTION OF NORMAL MODE PROBLEM AND ITS APPLICATION

5.1 Equations of the Eigenvalue-problem and an Accurate Mode Superposition

In Section 2, an asymmetric NMM problem in the spherical coordinates is constructed from a given bathymetry, and an experiential normalization equation (2.16) is used. Here, a novel approach allows us to construct a symmetric one in the spherical coordinates, with an accurate normalization equation (5.11). Similar as in the Cartesian coordinates case, a symmetric construction has the following advantages over asymmetric one: 1) Faster time to solve. 2) Less storage requirement. 3) Achieving true orthogonality. Instead of constructing a standard eigenvalue-problem which has the form of equation (2.9), a generalized eigenvalue-problem equation (5.2) is constructed first. Using its special property, it is converted to a standard eigenvalue-problem equation (5.7), which is faster to be solved than the original generalized eigenvalue-problem.

In the spherical coordinates, equation (2.5) can be written as:

$$\frac{\partial}{\partial\theta}\left(D\,sin\,\theta\,\frac{\partial h}{\partial\theta}\right)+\frac{1}{sin\,\theta}\frac{\partial}{\partial\varphi}\left(D\,\frac{\partial h}{\partial\varphi}\right)=\lambda R^2\,sin\,\theta\,h \quad (5.1)$$

which is equivalent to a generalized eigenvalue problem:

$$\boldsymbol{Ah}=\lambda\boldsymbol{Bh} \quad (5.2)$$

In a staggered grid system, $\boldsymbol{A}$ and $\boldsymbol{B}$ have the following forms:

$$A_{ij,i'j'}=\frac{\delta_{j,j'}}{\Delta\theta^2}\left[D_{i+1/2,j}\,sin\,\theta_{i+1/2}\left(\delta_{i+1,i'}-\delta_{i,i'}\right)-D_{i-1/2,j}\,sin\,\theta_{i-1/2}\left(\delta_{i,i'}-\delta_{i-1,i'}\right)\right]+\frac{\delta_{i,i'}}{sin\theta_i\Delta\varphi^2}\left[D_{i,j+1/2}\left(\delta_{j+1,j'}-\delta_{j,j'}\right)-D_{i,j-1/2}\left(\delta_{j,j'}-\delta_{j-1,j'}\right)\right] \quad (5.3)$$

$$B_{ij,i'j'}=R^2\,sin\,\theta_i\,\delta_{ii'}\delta_{jj'} \quad (5.4)$$

Here $\boldsymbol{A}$ is a symmetric matrix and $\boldsymbol{B}$ is a diagonal matrix. Conducting Cholesky decomposition to $\boldsymbol{B}$:

$$\boldsymbol{B}=\boldsymbol{R^TR} \quad (5.5)$$

we have

$$(\boldsymbol{R^T})^{-1}\boldsymbol{AR^{-1}Rh}=\lambda\boldsymbol{Rh} \quad (5.6)$$

which can be reduced to

$$\boldsymbol{Eh'}=\lambda\boldsymbol{h'} \quad (5.7)$$

where $\boldsymbol{E}=(\boldsymbol{R^T})^{-1}\boldsymbol{AR^{-1}}$ and $\boldsymbol{h'}=\boldsymbol{Rh}$. This is the eigenvalue-problem to solve. Because $\boldsymbol{E}$ is also a symmetric matrix, the above equation (5.7) is a symmetric eigenvalue-problem.

Because $\boldsymbol{B}$ is a diagonal matrix, $\boldsymbol{R}$ is also a diagonal matrix and can be deduced from $\boldsymbol{B}$ easily:

$$R_{ij,i'j'}=\sqrt{R^2\,sin\,\theta_i}\,\delta_{ii'}\delta_{jj'} \quad (5.8)$$

Other terms are therefore obtained:

$$E_{ij,i'j'} = \frac{\delta_{j,j'}}{R^2\sqrt{\sin\theta_i \sin\theta_{i'}}\Delta\theta^2}\left[D_{i+1/2,j}\sin\theta_{i+1/2}\left(\delta_{i+1,i'} - \delta_{i,i'}\right) - D_{i-1/2,j}\sin\theta_{i-1/2}\left(\delta_{i,i'} - \delta_{i-1,i'}\right)\right] + \frac{\delta_{i,i'}}{R^2 sin^2\theta_i \Delta\varphi^2}\left[D_{i,j+1/2}\left(\delta_{j+1,j'} - \delta_{j,j'}\right) - D_{i,j-1/2}\left(\delta_{j,j'} - \delta_{j-1,j'}\right)\right] \quad (5.9)$$

$$h'_{i,j} = \sqrt{R^2 \sin\theta_i}\, h_{i,j} \quad (5.10)$$

The orthogonality of the eigenvectors $\boldsymbol{h}$ in (5.2) is $\boldsymbol{B}$ based, that is:

$$\boldsymbol{h}_i^T \boldsymbol{B} \boldsymbol{h}_j = \delta_{ij} \quad (5.11)$$

where δ_{ij} is the Kronecker delta.

Then from the superposition of the normal modes:

$$\eta(\boldsymbol{x}, t) = \sum_i C_i h_i(\boldsymbol{x}) cos\omega_i t \quad (5.12)$$

where h_i can be easily deduced from h'_i.

And from the initial condition $\eta_0(\boldsymbol{x})$ when t=0, we can calculate the coefficient:

$$C_i = \boldsymbol{h_i^T B \eta}_0 = \boldsymbol{h_i^T R^T R \eta}_0 = \boldsymbol{h'^T R \eta}_0 \quad (5.13)$$

Table 5.1 shows a quick comparison of the time needed to solve the "same" eigenvalue-problem between a symmetric one and an asymmetric one. When the required number of modes grows, there is a significant advantage of the symmetric one.

Table 5.1 Basic comparison of calculation time between symmetric and asymmetric mode solving methods of the same 2 arc-min Sea of Japan

Num. modes obtained	CPU Time Symmetric (s)	CPU Time Asymmetric (s)
100	2678	2910
200	4911	5080
400	12133	14277
800	33908	81613

5.2 Modal Solution Calculation Results

Solving the symmetric eigenvalue-problem constructed in Section 5.1 using the same 2 arc-min as in Section 2.3 and a symmetric solver of the same Arpack library mentioned in Section 2.2, 15,000 modes (period down to 5 min) are obtained, which is totally difficult when the problem is asymmetric.

Table 5.2 shows the calculation time to obtain a specific number of modes, and the shortest period of the modes that can be obtained through that computation, based on a symmetric problem construction. Comparing to the asymmetric one in Section 2.3, which took 15.2 days to obtain 6,000 modes, the new approach can double the number of modes with the same computation time.

Table 5.2 Calculation results of modal solutions of the 2 arc-min Sea of Japan, using a symmetric problem construction.

Num. modes obtained	Shortest period (min)	Calculation time (day)
6000	8.5	6.7
9500	6.6	11.9
12000	5.7	15.5
15000	5.0	20.4

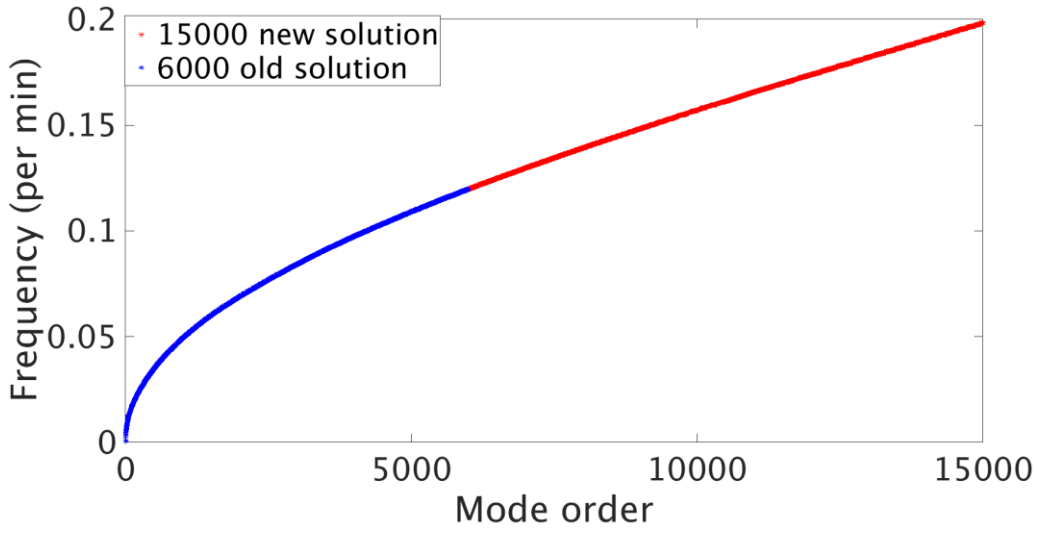

Figure 5.1 The relation between the mode order and their frequency for the symmetric approach. The asymmetric approach result in Section 2 is also plotted as a reference. Notice the overlay of the first 6000 modes: this indicates that the new numerical calculation is valid, and the accuracy is at least not less than using the asymmetric one.

5.3 Synthesized Waveforms and their Properties

Using the obtained 15,000 normal modes of the Sea of Japan, tsunami waveforms generated by the 1983 Sea of Japan earthquake are simulated, similar to in Section 3.2. The results are shown in Figure 5.2.

For Iwanai, since the simulation was already good, the new synthetized waveform improves a little near the peaks around 40 min and 90 min. For Saigo, the synthetic waveform using 15,000 modes in general matches FDM waveform well, which improves significantly over the waveform synthetized by the 6,000 modes. The latter does not cover high frequency energy at all. This indicates that the novel modal solution covers the usual frequency band of tsunami waveforms in the Sea of Japan.

For Kustugata, the waveform is almost identical to the 6,000 asymmetric based modal result, which means that the latter is already the "final" waveform. Therefore, as mentioned in Section 3.2, the discrepancy is probably due either to being located close to the node boundary or to being located where the bathymetry changes rather dramatically. Further investigations show that if using a finer bathymetry (1-arc-min) to do FDM simulation (Figure 5.3a), or just shifting the location of Kutsugata in the original 2-arc-min FDM simulation by one grid (Figure 5.3b), we can get far better match. These results suggest that, while the node boundary may still be a reason, the discrepancy is more likely due to the dramatic bathymetry change.

Besides, an important improvement in the leading wave part can be observed. Figure 5.4 shows the enlarged leading wave part of Iwanai, Kutsugata and Saigo. To ensure fairness, symmetric and asymmetric NMM simulated waveforms are both using 6,000 modes (using 15,000 modes makes the waveforms even better). First, we can observe that in the new synthetic waveforms have almost no energy before the initial arrival. In contrast, for example at Iwanai, the asymmetric solution has unignorable energy starting from the beginning till around 15 min and also around 25 min. Besides, the new synthetic waveforms have better agreements to FDM around the onset. This is more notable at Kutsugata, where the asymmetric solution has a five-minute earlier onset.

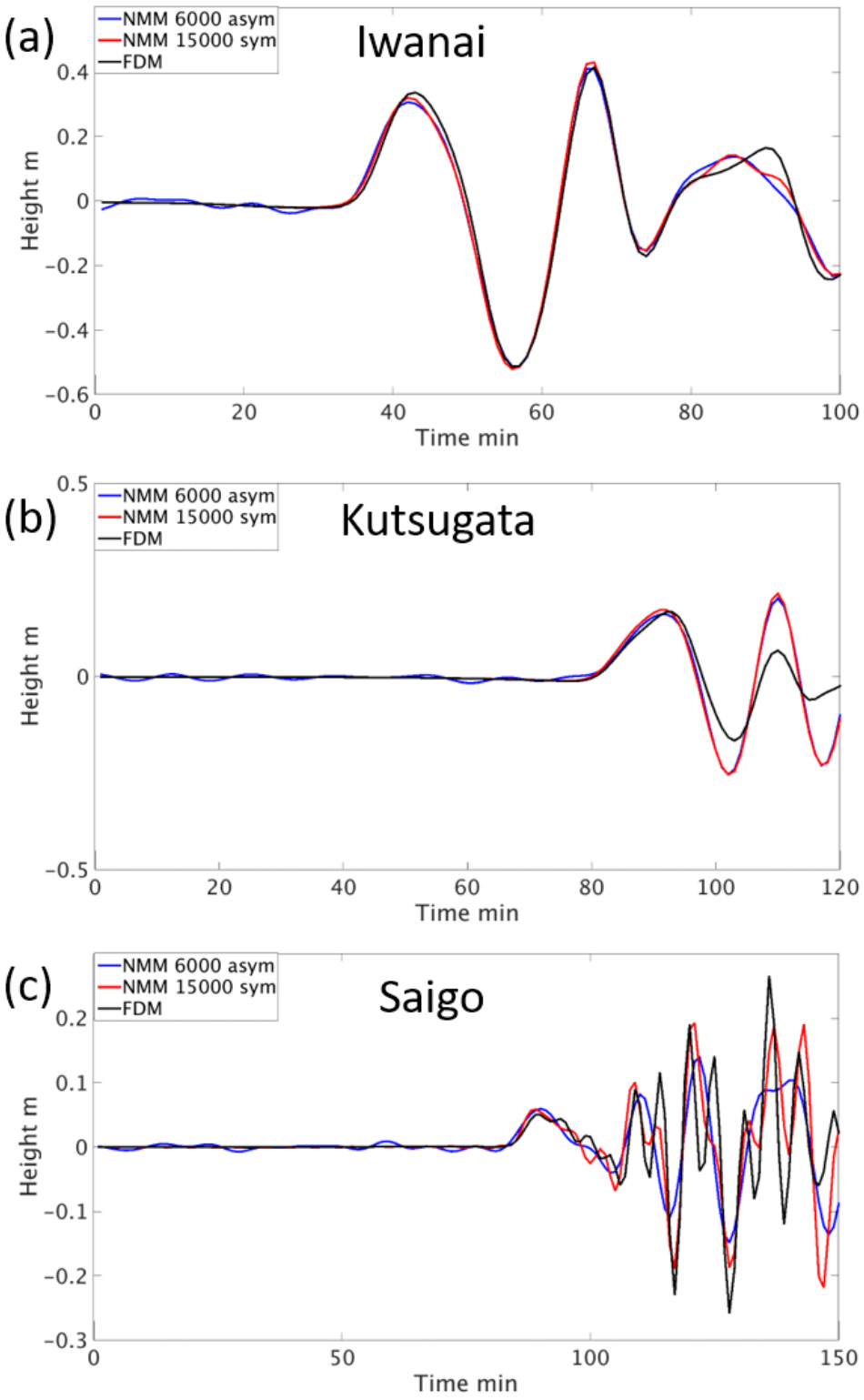

Figure 5.2 Waveforms simulated by 15,000 modes from symmetric NMM construction. The simulations from former asymmetric NMM construction and FDM are also shown.

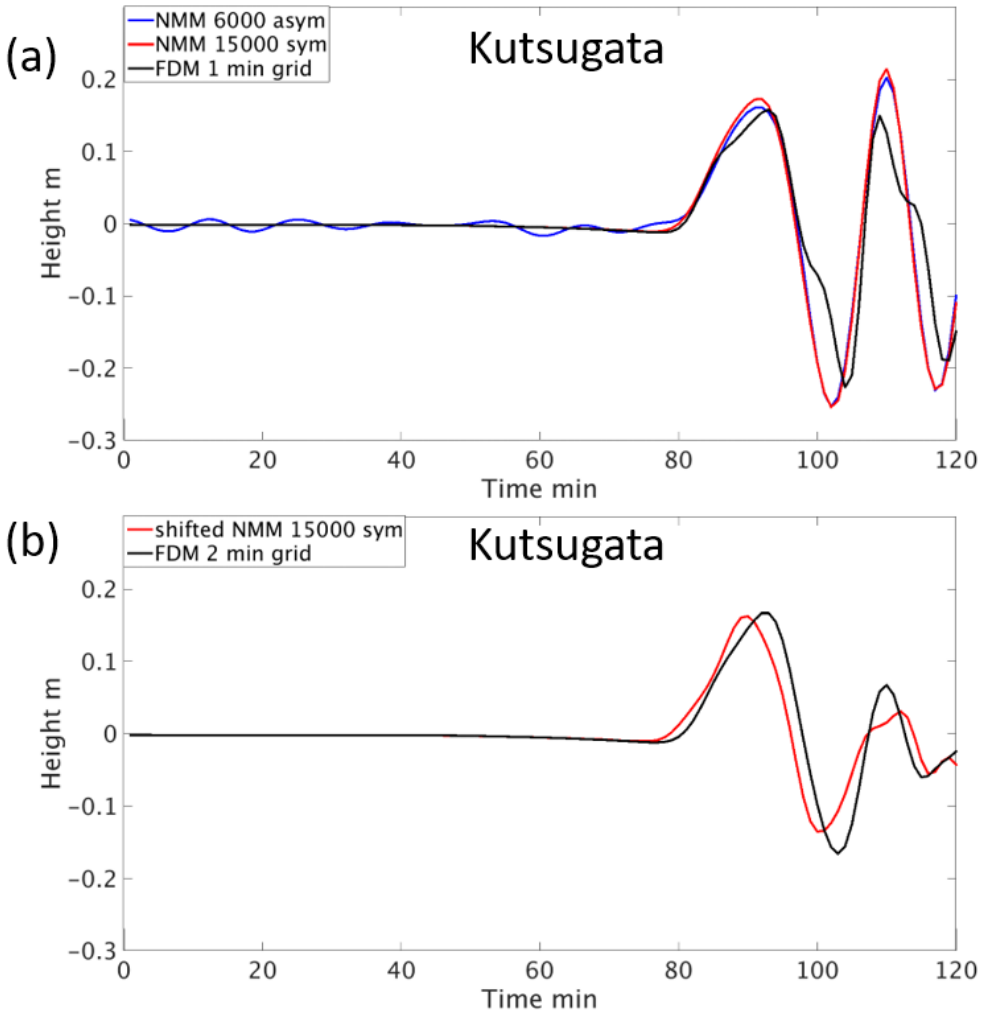

Figure 5.3 (a) At Kutsugata. The same as Figure 5.2 (b), but the FDM result is from a 1 arc-min grid instead of a 2 arc-min one. (b) At Kutsugata. Comparison between FDM simulated result in Figure 3.1 and simulated waveform by 15,000 modes from symmetric NMM construction, with one grid shift from the Kutsugata location in Figure 3.1.

It is of interest to notice that, if we multiply $\boldsymbol{B^{-1}}$ to both side of equation (5.2), we obtain equation (2.15), the asymmetric eigenvalue-problem, while equation (5.7), the symmetric eigenvalue-problem we are solving, is also deduced from eq. (5.2). The two problems should be therefore identical. As shown in Figure 5.1, the eigenvalues are exactly the same.

Therefore, the differences are only due to the choice of normalization equations. The former results in Section 3 are based on the experiential normalization equation (2.16), which ignores the changes of $\boldsymbol{dx}$ term in (2.6), while in the novel approach, accurate normalization (5.11) is used, where the $\boldsymbol{B}$ matrix incorporates the $\boldsymbol{dx}$ term. And when

the region of interest is reasonably small (like the Sea of Japan case), ***B*** is close to an identical matrix (multiplied by a constant). That is why we can get reasonable solutions even by using an experiential normalization equation (2.16).

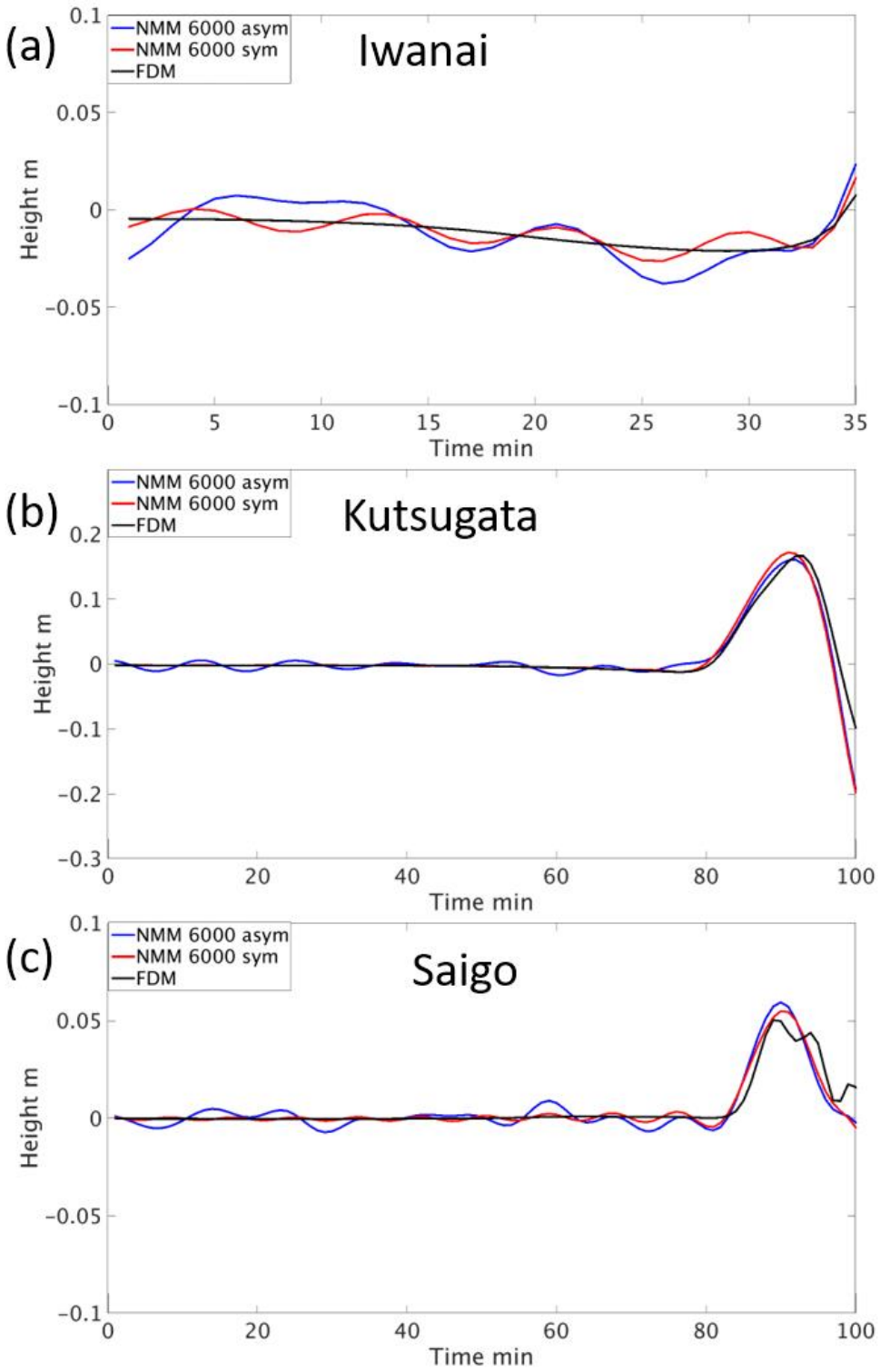

Figure 5.4 Comparison between initial phases simulated by modes from symmetric NMM construction and from the asymmetric one. Number of modes used are both 6,000 to ensure fairness. FDM results are also shown as a reference.

6 PERSPECTIVES TOWARDS A MODAL SOLUTION OF THE GLOBAL OCEAN

6.1 Using Shift Method to Obtain Higher Modes Directly

For matrix $\boldsymbol{A}$ and $\boldsymbol{B} = \boldsymbol{A} - p\boldsymbol{I}$, where I is the unit matrix and p is a given scalar number, if $\boldsymbol{B}$ has eigenvalues λ_i, then $\boldsymbol{A}$ has eigenvalues $\lambda_i + p$, and the corresponding eigenfunctions are the same. Because iteration methods can only obtain extreme eigen-pairs (ex. eigen-pairs with largest eigenvalues), applying a shift p to the origin matrix $\boldsymbol{A}$ will enable the calculation of higher modes directly. This is useful when combined with parallel computing.

For the 2-arc-min Sea of Japan case, applying shift to obtain around 180 modes from the 6,000th modes takes about 67 hours using 32 cores on EIC computer system. Therefore this approach is not fast but still affordable.

6.2 NMM Equations with Elastic Loading, Gravitational Potential Change and Seawater Compressibility

Watada et al. (2014) demonstrated the importance of elastic loading, gravitational potential change and seawater compressibility when considering far-field tsunami propagations. Trans-Pacific tsunamis may be delayed up to 15 minutes with an initial phase reversal due to these effects. In order to achieve better far field simulation results, it is desirable to take these effects into account.

Elastic loading and gravitational potential change are referred to as self-attraction and loading (SAL) effects in the field of physical oceanography (Baba et al, 2017). That is, when a mass loads the Earth, its gravity field will be changed through crustal deformation and self-gravitation processes.

Linear shallow-water equations considering SAL effects has the following form (Allgeyer & Cummins, 2014)

$$\frac{\partial \boldsymbol{V}}{\partial t} = -g\nabla\eta \quad (6.1a)$$

$$\frac{\partial(\eta+\xi)}{\partial t} = -\nabla\cdot(D\boldsymbol{V}) \quad (6.1b)$$

This is identical with equation (2.1) except that the displacement of the ocean floor ξ is also taken into account. Notice that seawater compressibility of the ocean may also be considered (Tsai et al, 2013), with (6.1b) modified to:

$$\rho_H \frac{\partial(\eta+\xi)}{\partial t} = -\rho_{avg}\nabla\cdot(D\boldsymbol{V})$$

where ρ_H is the water density at the sea floor and ρ_{avg} is the average water density. Here, we only discuss the case of (6.1b), and the seawater compressibility case is similar.

Using a similar process described in Section 2.1.1, we can get one second order differential equation:

$$\frac{\partial^2(\eta+\xi)}{\partial t^2} = g\nabla\cdot(D\nabla\eta) \quad (6.2)$$

The earth's response ξ to SAL effects can be calculated using a Green's function (Vinogradova et al., 2015), which represents the response at $\boldsymbol{r}'$ to a unit mass loading at a given surface point $\boldsymbol{r}$:

$$G(\boldsymbol{r}', \boldsymbol{r}) = G(\alpha) = \frac{-R}{M_e} \sum_{n=0}^{\infty} (1 + k_n' - h_n') P_n(cos\alpha)$$

where P_n is the *n*th Legendre polynomial, α is the angular distance between the loading point and the response point, *R* is the radius of the earth, M_e is the mass of the earth and k_n' and h_n' are the loading Love number of angular order *n*.

Then ξ can be calculated from a convolution of the height of the water column and the corresponding Green's function (Hendershott, 1972):

$$\xi(\boldsymbol{r}) = \iint G(\boldsymbol{r}', \boldsymbol{r})[\eta(\boldsymbol{r}') + \xi(\boldsymbol{r}')]dS$$

While we have $\xi(\boldsymbol{r}') << \eta(\boldsymbol{r}')$, the equation now becomes:

$$\xi(\boldsymbol{r}) = \iint G(\boldsymbol{r}', \boldsymbol{r})\eta(\boldsymbol{r}')dS$$

And equation (6.2) becomes:

$$\frac{\partial^2(\eta + \iint G(\boldsymbol{r}', \boldsymbol{r})\eta(\boldsymbol{r}')dS)}{\partial t^2} = g\nabla \cdot (D\nabla\eta)$$

Then the only difference with equation (2.2) is that the left side is now the differentiation of the linear combination of η over the space, instead of just η. Similarly, if we substitute $\eta(\boldsymbol{x}, t) = e^{i\omega t}h(\boldsymbol{x})$, then we can get the following eigenvalue-problem:

$$\left(h + \iint G(\boldsymbol{r}', \boldsymbol{r})h(\boldsymbol{r}')dS\right) = -\frac{g}{\omega^2}\nabla \cdot (D\nabla\eta)$$

or

$$\nabla \cdot (D\nabla h) = \lambda(h + \iint G(\boldsymbol{r}', \boldsymbol{r})h(\boldsymbol{r}')dS)$$

where $\lambda = -\frac{\omega^2}{g}$.

This has a discrete matrix form of:

$$\boldsymbol{Ah}=\lambda\boldsymbol{Bh} \quad (6.3)$$

Here, $\boldsymbol{A}$ is the discretization of $\nabla \cdot D\nabla$, and $\boldsymbol{B}$ is a matrix representing a correction due to the elastic loading. This is a generalized eigenvalue-problem and can be solved by many numerical libraries including Arpack. Notice that although equation (6.3) has the same form as equation (5.2), it cannot be transformed to a standard eigenvalue-problem because $\boldsymbol{B}$ here is not a diagonal matrix.

The orthogonality of the eigenvectors $\boldsymbol{h}$, same as equation (5.11) is $\boldsymbol{B}$ based orthogonal, that is:

$$\boldsymbol{h}_i^T \boldsymbol{B} \boldsymbol{h}_j = \delta_{ij}$$

where δ_{ij} is the Kronecker delta.

Then from the superposition of the normal modes is the same as equation (5.12):

$$\eta(\boldsymbol{x}, t) = \sum_i C_i h_i(\boldsymbol{x}) cos\omega_i t$$

and the initial condition $\eta_0(\boldsymbol{x})$ when t=0, we can calculate the coefficient similar to equation (5.13):

$$C_i = h_i \boldsymbol{B} \eta_0$$

6.3 NMM Equations with Coriolis Force

For far-field tsunamis, since the travel time is comparable with the earth's rotation period, the Coriolis force may have nonnegligible influences. Therefore, Coriolis Force is worthwhile to taken into account.

The linear shallow-water equations with Coriolis force are:

$$\frac{\partial \boldsymbol{V}}{\partial t} = -g\nabla\eta - 2\boldsymbol{\Omega} \times \boldsymbol{V}$$

$$\frac{\partial \eta}{\partial t} = -\nabla \cdot (D\boldsymbol{V})$$

Where the $-2\boldsymbol{\Omega} \times \boldsymbol{V}$ term is the term related to Coriolis force. The linearity of the equations enables the possibility of using NMM, while the cross product makes the problem more difficult. One way to deal with the problem is to use first order differential equations instead of one second order differential equation, and to use scalar potentials to replace the velocity vectors. In Platzman (1978), Stokes/Helmholtz potentials are used:

$$\boldsymbol{V} = p(\varphi) + q(\psi)$$

$$p(\varphi) = -\nabla\varphi$$

$$q(\psi) = \frac{k}{D} \times \nabla\psi$$

And then an eigenvalue-problem can be constructed:

$$-i\boldsymbol{A}X = \omega\boldsymbol{B}\boldsymbol{X}$$

Here, the vector $\boldsymbol{X}$ is the eigenvector representing η, φ and ψ. $\boldsymbol{A}$ and $\boldsymbol{B}$ are matrix constructed from the bathymetry and Coriolis force. This is a generalized eigenvalue-problem similar to (5.3), whose solution is:

$$x(t) = Re(Xe^{i\omega t})$$

where *x* consists of η, φ and ψ.

6.4 Potential and Future of NMM

In this study, necessary tools for conducting NMM calculation and analysis are developed as well as a careful examination of their properties. We have seen that the agreement of waveforms simulated by the NMM and FDM depends on the number of modes. Therefore, to compute waveforms at shorter periods, calculation of more modes will be the key to further development of this method. It is also of interest to obtain the normal-mode solutions for larger areas like the Mediterranean Sea, which is roughly 2.5

times as large as the Sea of Japan. (Actually the calculation for the Mediterranean Sea in 2-arc-min grids is already possible).

Ultimately, we may be able to perform this analysis for the whole global ocean. In this case, we may need to include both the Coriolis force and elasticity effect of the Earth. These makes the computation more complicated: we need to solve a generalized eigenvalue-problem and the matrix may no longer be sparse. A recent record for solving dense-matrix eigenvalue-problems was set by the K-computer, which solved a 1 million by 1 million dense matrix in 1 hour (Imamura & Yamamoto, 2014). The global ocean is around 350 times larger than the Sea of Japan. If we use 10-arc-min grids instead of 2-arc-min grids, there will be around 14 times more ocean grids. This makes the dimension n of the eigenvalue matrix also 14 times larger, which has the order of 1 million. So in the near future, it may be possible to obtain normal-mode solutions for the global ocean. The merit for obtaining such a solution for the world ocean is huge: normal FDM simulation of a trans-Pacific tsunami take hours of calculation time while NMM mode superposition takes only seconds of time, as shown in Section 3.5. Besides, waveform data from deep ocean pressure gauges are available. Instead of tide gauges, high frequency energy is limited at these pressure gauges and therefore suitable for the property of the NMM.

When more powerful computers and algorithms become available in the future, the NMM may become a very powerful tool for tsunami numerical computation.

7 CONCLUSION

Important problems of the tsunami NMM were solved, together with some powerful tools were provided to conduct and analyze NMM calculation of a region.

First, the previous NMM was converted into a spherical coordinate system together with an experiential normalization way to simplify the numerical calculation. Then implementations of linear matrix storage, matrix-vector multiplication a modern sparse eigenvalue solver made the calculation of large scale NMM problems realistic. A parallel version of the calculation was also developed.

Then, 6,000 normal-mode solutions were obtained for the Sea of Japan with a grid interval of 2 arc-min, as well as 3,000 modal solutions for 1-arc-min grids using parallel computing. Using these fine modal solutions, tsunami waveforms were synthesized by the NMM for what the authors believe to be the first time: tsunami waveforms generated by the Mw 7.7 Sea of Japan earthquake were computed. Comparison with the results from the FDM and examination in both time and frequency domains confirmed the validity of the NMM when the modes cover the frequency range of the signal.

Measurement showed that waveform simulation time of original NMM is faster than that of FDM, but the advantage is not significant. A way to accelerate NMM waveform simulation time was proposed and enables the calculation time faster than FDM by

several orders even in a moderate region like the Sea of Japan, which further strengthens the advantage of the NMM. Besides, a relationship between the mode order and the mode frequency was proposed so that it is possible to estimate the number of modes to calculate in advance. And based on this relationship, a method to estimate the required modes for simulation waveforms at a given place was also proposed.

In addition, unique to the traditional modal analysis, in this study, the NMM was also used to characterize tsunami sources with excitation weights. This study included calculation of the excitation weights of 60 potential submarine faults in the Sea of Japan, as determined by MLIT. With the help of kurtosis, modes were divided into three groups: basin-wide, regional, and local groups. These excitation weights suggested that sources located at shallower water depths have the potential to generate larger regional modes, which made the largest contribution among the three kinds of modes and could significantly affect coastal areas.

Finally, a practical NMM in the Sea of Japan in the spherical coordinates was proposed: a symmetric NMM eigenvalue-problem construction together with accurate mode normalization and superposition equations. The symmetric approach enabled faster and better calculation of modal solution, which yielded modal solutions of the Sea of Japan down to 5 min in period. Using these modal solutions, tsunami waveforms synthetized by mode superposition can cover the usual frequency band in the Sea of Japan. Besides, the accurate mode normalization resulted almost no energy before the initial arrival and better agreements to FDM around the onset.

In the future, it is of interest to calculate the modal solution of a larger area. The Mediterranean Sea, whose size is about 2.5 times of the Sea of Japan, can already be handled. Ultimately, with the development of matrix eigenvalue-problem solver, the modal solution of the world ocean may also be obtained.

8 REFERENCES

Aida, I (1996), Characteristics of Tsunamis Caused by Earthquakes beneath the Tokyo Bay Area. Journal of the Seismological Society of Japan (Zisin), 49(2), 217-226. (in Japanese with English abstract)

Allgeyer, S., and Cummins, P. (2014), Numerical tsunami simulation including elastic loading and seawater density stratification, *Geophysical Research Letters*, 41, 2368–2375, doi:10.1002/2014GL059348

Baba, T., Allgeyer, S., Hossen, J., Cummins, P., Tsushima, H., Imai, K., Yamashita, K., Kato, T. (2017), Accurate numerical simulation of the far-field tsunami caused by the 2011 Tohoku earthquake, including the effects of Boussinesq dispersion, seawater density stratification, elastic loading, and gravitational potential change, *Ocean Modelling*, 111, 46-54,

Bellotti, G., R. Briganti, G. M. Beltrami, and F. Leopoldo (2012a), Modal analysis of semi‐enclosed basins, *Coastal Engineering*, 64, 16–25

Bellotti, G., Briganti, R. & Beltrami, G. M. (2012b), The combined role of bay and shelf modes in tsunami amplification along the coast. *Journal of Geophysical Research,* 117(C8)

Cortés, P., P. A. Catalán, R. Aránguiz, and G. Bellotti (2017), Tsunami and shelf resonance on the northern Chile coast, *Journal of Geophysical Research, Oceans*, 122, 7364–7379, doi: 10.1002/2017JC012922

Dziewonski, A. M. & Woodhouse, J. H. (1983). An experiment in systematic study of global seismicity: Centroid‐moment tensor solutions for 201 moderate and large earthquakes of 1981. *Journal of Geophysical Research*, 88(B4), 3247-3271

Heidarzadeh, M. & Satake, K. (2014). Excitation of Basin-Wide Modes of the Pacific Ocean Following the March 2011 Tohoku Tsunami, *Pure and Applied Geophysics*, 171: 3405. https://doi.org/10.1007/s00024-013-0731-5

Hendershott, M. C. (1972) The Effects of Solid Earth Deformation on Global Ocean Tides, Geophysical Journal International, Volume 29, Issue 4, Pages 389–402, https://doi.org/10.1111/j.1365-246X.1972.tb06167.x

Imamura, T. & Yamamoto, Y. (2014) "CREST: Dense Eigen-Engine Groups", International Workshop on Eigenvalue Problems: Algorithms; Software and Applications, in Petascale Computing, Tsukuba, March 7–9, 2014 (poster), http://www.aics.riken.jp/labs/lpnctrt/assets/img/EPASA2014_dense_poster_ImamuraT_only.pdf

Intergovernmental Oceanographic Commission, International Hydrographic Organization, and British Oceanographic Data Centre (2003), Centenary Edition of the GEBCO Digital Atlas, published on CD- ROM on behalf of the Intergovernmental Oceanographic Commission and the International Hydrographic Organization as part of the general bathymetric chart of the oceans. British oceanographic data centre, Liverpool, U. K.

Irikura, K. and Miyake, H. (2001). Prediction of strong ground motions for scenario earthquakes. *Journal of Geography (Chigaku Zasshi)* 110 (6), 849-875. (in Japanese with English abstract)

Japan Meteorological Agency (1984), Report on the Nihonkai-Chubu Earthquake, 1983 (in Japanese), *Technical Report of the Japan Meteorological Agency*, No. 106, ISSN 0447-3868

Lehoucq, R. B., Sorensen D. C. & Yang C. (1996), APPACK user's guide: Solution of large scale eigenvalue problems by implicitly restarted Arnoldi methods, technical report, Dep. of Comput. and Appl. Math., Rice Univ., Houston, Tex.

Loomis, H. G. (1973), A new method for determining normal modes of irregular bodies of water with variable depth. *Hawaii Institute of Geophysics*, HIG–73–10, NOAA–JTRE–86, 27pp

Loomis, H. G. (1975), Normal modes of oscillation of Honokohau harbor, Hawaii. *Hawaii Institute of Geophysics* , HIG–75–20, NOAA–JTRE–142

Maschhoff K.J., Sorensen D.C. (1996) P_ARPACK: An efficient portable large scale eigenvalue package for distributed memory parallel architectures. In: Waśniewski J., Dongarra J., Madsen K., Olesen D. (eds) Applied Parallel Computing Industrial Computation and Optimization. PARA 1996. Lecture Notes in Computer Science, vol 1184. Springer, Berlin, Heidelberg

Ministry of Land, Infrastructure, Transport and Tourism (MLIT) (2014), Report of Investigation Committee for Large-scale Earthquakes in Japan Sea (in Japanese), 470 pp., https://www.mlit.go.jp/river/shinngikai_blog/daikibojishinchousa/houkoku/Report.pdf

Müller, M. (2007), The free oscillations of the world ocean in the period range 8 to 165 hours including the full loading effect. *Geophysical Research Letters,* 34, L05606

Okada, Y. (1985), Surface deformation due to Shear and Tensile Faults in a Half-space. *Bulletin of the Seismological Society of America,* 75, 1135-1154

Platzman, G. W. (1978), Normal modes of the world ocean. Part I: Design of a finite-element barotropic model. *Journal of Physical Oceanography*, 8(3), 323-343

Platzman, G. W., Curtis, G. A., Hansen, K. S. and Slater, R. D. (1981), Normal modes of the world ocean. Part II: Description of modes in the period range 8 to 80 hours. *Journal of Physical Oceanography*, 11(5), 579-603

Platzman, G. W. (1984a), Normal modes of the world ocean. Part III: A procedure for tidal synthesis. *Journal of Physical Oceanography*, 14(10), 1521-1531

Platzman, G. W. (1984b), Normal modes of the world ocean. Part IV: Synthesis of diurnal and semidiurnal tides. *Journal of Physical Oceanography*, 14(10), 1532-1550

Rabinovich, A. B. (2009), Seiches and harbor oscillations, in Handbook of Coastal and Ocean Engineering, edited by Y. C. Kim, pp. 193-236, World Sci., Singapore

Sanchez, B. V. (2008), Normal modes of the global oceans—a review. *Marine Geodesy*, 31(3), 181-212

Satake, K, (1985), The mechanism of the 1983 Japan Sea earthquake as inferred from long-period surface waves and tsunamis, *Physics of the Earth and Planetary Interiors*, 37, 249-260

Satake, K, (1995) Linear and non-linear computations of the 1992 Nicaragua earthquake tsunami. *Pure and Applied Geophysics*, 144, 455-470

Satake, K. and Shimazaki, K. (1987), Computation of tsunami waveforms by a superposition of normal modes. *Journal of Physics of the Earth*, 35(5), 409-414

Satake, K. and Shimazaki, K. (1988), Free oscillations of the Japan Sea excited by earthquakes—Ⅱ. Modal approach and synthetic tsunamis. *Geophysical Journal*, 93(3), 457-463

Takigawa, A. (2015), Tsunami Heights and Period Distribution of Tokyo Bay and Characteristic Oscillation of Tokyo and Sagami Bays, Master Thesis, Department of Earth and Planetary Science, Faculty of Science, The University of Tokyo.

Tsai, V. C., J.‐P. Ampuero, H. Kanamori, and D. J. Stevenson (2013), Estimating the effect of Earth elasticity and variable water density on tsunami speeds, Geophys. Res. Lett., 40, 492–496, doi: 10.1002/grl.50147

Vinogradova, N.T., Ponte, R.M., Quinn, K.J., Tamisiea, M.E., Campin, J.-M., Davis, J.L., Dynamic adjustment of the ocean circulation to self-attraction and loading effects. *J. Phys. Oceano.*, 45 (2015), pp. 678-689, 10.1175/JPO-D-14-0150.1

Watada, S. and Kanamori, H. (2010), Acoustic resonant oscillations between the atmosphere and the solid earth during the 1991 Mt. Pinatubo eruption. *Journal of Geophysical Research*, 115, B12319, doi:10.1029/2010JB00774

Watada, S, Kusumoto, S and Satake, K, (2014) Traveltime delay and initial phase reversal of distant tsunamis coupled with the self-gravitating elastic Earth, *Journal of Geophysical Research: Solid Earth*, 119, 5, 4287

Watanabe, H. (1998), Comprehensive List of Destructive Tsunamis in Japan (Nihon Higai Tsunami Soran) 2nd edition, Univ. Tokyo Press, 238 pp. (In Japanese)

Wu, Y. and Satake, K. (2018), Synthesis and source characteristics of tsunamis in the Sea of Japan based on normal-mode method, *Journal of Geophysical Research: Solid Earth*, 123, 5760–5773

Yalciner, A.C., and Pelinovsky, E.F. (2007). A short cut numerical method for determination of periods of free oscillations for basins with irregular geometry and bathymetry, Ocean Eng., 34, 5-6, 747–757

APPENDIX A: FAULT PARAMETERS OF 60 MLIT SUBMARINE FAULTS

Fault number No.	Mw	Length (km)	width (km)	Top depth (km)	Strike (degree)	Dip (degree)	rake (degree)	Average slip (m)	Latitude	Longitude
F01	7.88	46.5	7.0	1.1	340	45	78	6.00	44.8177	141.7569
		47.9	7.0		351	45	84		45.2075	141.5506
		67.6	7.0		342	45	79		45.6343	141.4535
		46.5	18.0	6.0	340	30	84		44.8329	141.8155
		47.9	18.0		351	30	88		45.2144	141.6126
		67.6	18.0		342	30	84		45.6480	141.5137
F02	7.67	53.7	19.3	1.4	355	45	82	5.18	45.1870	140.9505
		36.3	19.3		23	45	100		45.6630	140.8859
		27.6	19.3		7	45	89		45.9643	141.0736
F03	7.23	44.6	19.5	1.2	19	45	105	2.91	44.7424	140.5945
F04	7.33	58.4	18.8	1.7	34	45	138	3.28	44.7263	139.6710
F05	7.27	53.5	18.2	2.2	7	45	79	3.08	44.5380	139.3913
F06	7.61	42.0	19.1	1.5	217	45	82	4.73	44.3185	140.7304
		62.5	19.1		191	45	79		44.0135	140.4097
F07	7.42	29.0	17.9	2.4	176	45	54	3.70	44.5843	139.5556
		21.6	17.9		201	45	76		44.3286	139.5818
		25.3	17.9		167	45	48		44.1416	139.4856
F08	7.44	31.3	18.4	2.0	218	45	93	3.75	44.1467	140.1912
		20.9	18.4		189	45	77		43.9197	139.9500
		23.1	18.4		153	45	63		43.7285	139.9106
F09	7.61	24.4	27.9	4.0	347	30	103	4.78	43.6888	139.1853
		29.2	27.9		2	30	104		43.8979	139.1166
		18.8	27.9		347	30	103		44.1640	139.1298
F10	7.47	73.2	20.6	3.4	194	45	98	3.94	43.6878	139.6577
F11	7.48	78.1	19.5	4.2	180	45	67	3.97	43.9732	139.3373
F12	7.43	24.0	18.7	1.8	156	45	62	3.71	43.4047	139.8615
		29.3	18.7		161	45	65		43.2076	139.9794
		19.7	18.7		177	45	79		42.9607	140.0946
F13	7.34	53.4	21.2	3.0	172	45	70	3.33	42.6991	139.4869
F14	7.83	43.3	20.3	3.6	195	45	99	6.00	43.4326	139.5697
		79.6	20.3	3.6	192	45	111		43.0566	139.4315
		51.9	16.6	3.6	167	60	105		42.3542	139.2327
F15	7.83	45.2	20.1	3.8	173	45	97	6.00	43.4568	139.3648
		79.6	20.1	3.8	192	45	111		43.0566	139.4315
		51.9	16.4	3.8	167	60	105		42.3542	139.2327
F16	7.61	75.9	26.7	4.6	14	30	94	4.79	41.7417	138.6545
F17	7.78	53.9	21.5	2.8	10	45	106	6.00	41.0201	139.4058
		81.0	21.5		350	45	96		41.4998	139.5198
F18	7.71	100.0	18.1	2.2	7	45	95	5.52	40.8886	139.7757
		37.4	18.1		348	45	87		41.7824	139.9293
F19	7.77	58.6	27.3	4.3	33	30	110	6.00	40.8783	138.1776
		42.8	27.3		18	30	97		41.3225	138.5646
F20	7.80	30.8	18.4	2.0	151	45	68	6.00	41.4831	139.5716
		47.2	18.4	2.0	199	45	102		41.2482	139.7485
		52.4	18.4	2.0	165	45	103		40.8430	139.5615
		39.2	18.4	2.0	175	45	88		40.3887	139.7171
F21	7.44	30.8	17.9	2.4	151	45	68	3.76	41.4831	139.5716
		47.2	17.9		199	45	102		41.2482	139.7485
F22	7.34	63.9	17.5	2.6	1	45	98	3.31	40.9131	139.5750
F23	7.54	52.4	18.8	1.7	165	45	103	4.30	40.8430	139.5615
		39.2	18.8		175	45	88		40.3887	139.7171
F24	7.86	53.7	28.2	3.9	21	30	74	6.00	40.1054	138.9259
		77.9	28.2		349	30	80		40.5641	139.1542
F25	7.29	49.5	20.2	3.7	205	45	116	3.12	40.2604	138.7649
F26	7.43	70.9	19.4	1.3	184	45	85	3.73	39.9742	139.5708
F27	7.31	56.3	18.9	1.6	184	45	82	3.23	39.6464	138.9724
F28	7.67	35.7	18.0	2.3	200	45	115	5.18	40.0114	138.8859
		39.7	18.0		185	45	93		39.7079	138.7422
		50.9	18.0		202	45	118		39.3551	138.7060
F29	7.29	61.6	16.3	3.5	25	45	100	3.13	39.4819	138.3429
F30	7.79	96.1	19.3	1.3	202	45	98	6.00	39.8052	139.8661
		56.5	19.3		247	45	120		39.0100	139.4516

Fault number No.	Mw	Length (km)	width (km)	Top depth (km)	Strike (degree)	Dip (degree)	rake (degree)	Average slip (m)	Latitude	Longitude
F31	7.58	96.1	19.5	1.2	202	45	98	4.54	39.8052	139.8661
F32	7.32	56.5	19.0	1.5	247	45	120	3.24	39.0100	139.4516
F33	7.52	89.1	18.8	1.7	234	45	123	4.22	39.2937	139.3574
F34	7.71	71.9	19.7	1.1	211	45	106	5.45	39.0485	139.7337
		52.0	19.7		197	45	97		38.4894	139.3120
F35	7.58	99.1	19.2	1.4	200	45	96	4.59	38.9890	138.8728
F36	7.31	31.3	19.1	1.5	4	45	46	3.20	38.3432	138.2586
		23.6	19.1		36	45	97		38.6196	138.2837
F37	7.44	33.9	18.8	1.7	227	45	130	3.78	38.8706	138.4683
		41.0	18.8		185	45	90		38.6578	138.1766
F38	7.46	62.6	23.6	1.3	209	45	95	3.89	38.2341	138.7683
F39	7.42	37.3	18.0	2.3	350	45	67	3.67	37.7431	138.1239
		36.9	18.0		38	45	73		38.0658	138.0489
F40	7.19	14.7	18.9	1.6	26	45	84	2.80	37.4338	138.2858
		27.7	18.9		338	45	66		37.5605	138.3581
F41	7.60	51.5	22.7	1.9	37	45	76	4.66	36.9922	137.5859
		34.1	22.7		55	45	102		37.3618	137.9308
F42	7.28	37.7	17.7	2.5	201	45	78	3.10	38.0095	137.8939
		18.1	17.7		241	45	112		37.6983	137.7436
F43	7.57	48.3	19.7	1.1	64	45	113	4.50	37.3274	136.6811
		45.9	19.7		55	45	105		37.5179	137.1753
F44	7.27	36.0	19.6	1.2	230	45	99	3.08	37.9886	137.2724
		13.7	19.6		267	45	145		37.7836	136.9640
F45	7.18	16.2	18.3	2.0	228	45	103	2.77	37.2339	137.3179
		26.4	18.3		191	45	62		37.1319	137.1774
F46	6.85	26.0	13.0	1.1	177	60	42	2.05	37.0610	136.5533
F47	7.12	42.5	15.8	1.4	30	60	107	2.59	36.7282	136.0648
F48	6.91	28.2	14.1	2.1	81	60	215	2.14	37.0353	135.6625
F49	7.39	21.1	14.5	2.4	81	60	264	3.56	36.5243	134.8006
		36.3	14.5		47	60	145		36.5547	135.0374
		29.9	14.5		54	60	215		36.7748	135.3371
F50	6.78	23.7	11.8	1.2	39	60	126	1.95	36.4860	136.0401
F51	7.17	48.0	16.0	1.2	232	60	145	2.74	36.4332	136.0822
F52	7.34	22.5	16.1	1.1	319	60	35	3.34	35.7951	136.0921
		25.4	16.1		27	60	125		35.9418	135.9285
		22.5	16.1		344	60	40		36.1493	136.0572
F53	7.21	17.2	14.0	1.0	291	90	35	2.86	35.4324	135.9466
		11.4	14.0		310	90	35		35.4868	135.7681
		31.3	14.0		319	90	35		35.5523	135.6705
F54	7.19	57.6	13.9	1.1	332	90	35	2.80	35.5833	135.0833
F55	7.48	69.0	16.0	1.1	261	60	215	3.96	35.7569	134.4138
		25.8	16.0		249	60	215		35.6530	133.6580
F56	7.19	7.1	16.0	1.1	217	60	143	2.79	35.6189	132.9596
		42.4	16.0		268	60	215		35.5699	132.9171
F57	7.51	72.4	16.0	1.2	271	60	215	4.15	35.4992	132.4222
		30.1	16.0		235	60	145		35.5023	131.6174
F58	7.13	50.1	13.9	1.1	329	90	325	2.63	34.6586	131.5104
F59	7.38	87.9	13.9	1.1	310	90	325	3.49	34.1000	131.0833
F60	7.59	136.9	14.0	1.0	321	90	325	4.60	33.3933	130.8816

APPENDIX B: EXCITATION WEIGHTS OF THE 60 MLIT FAULTS

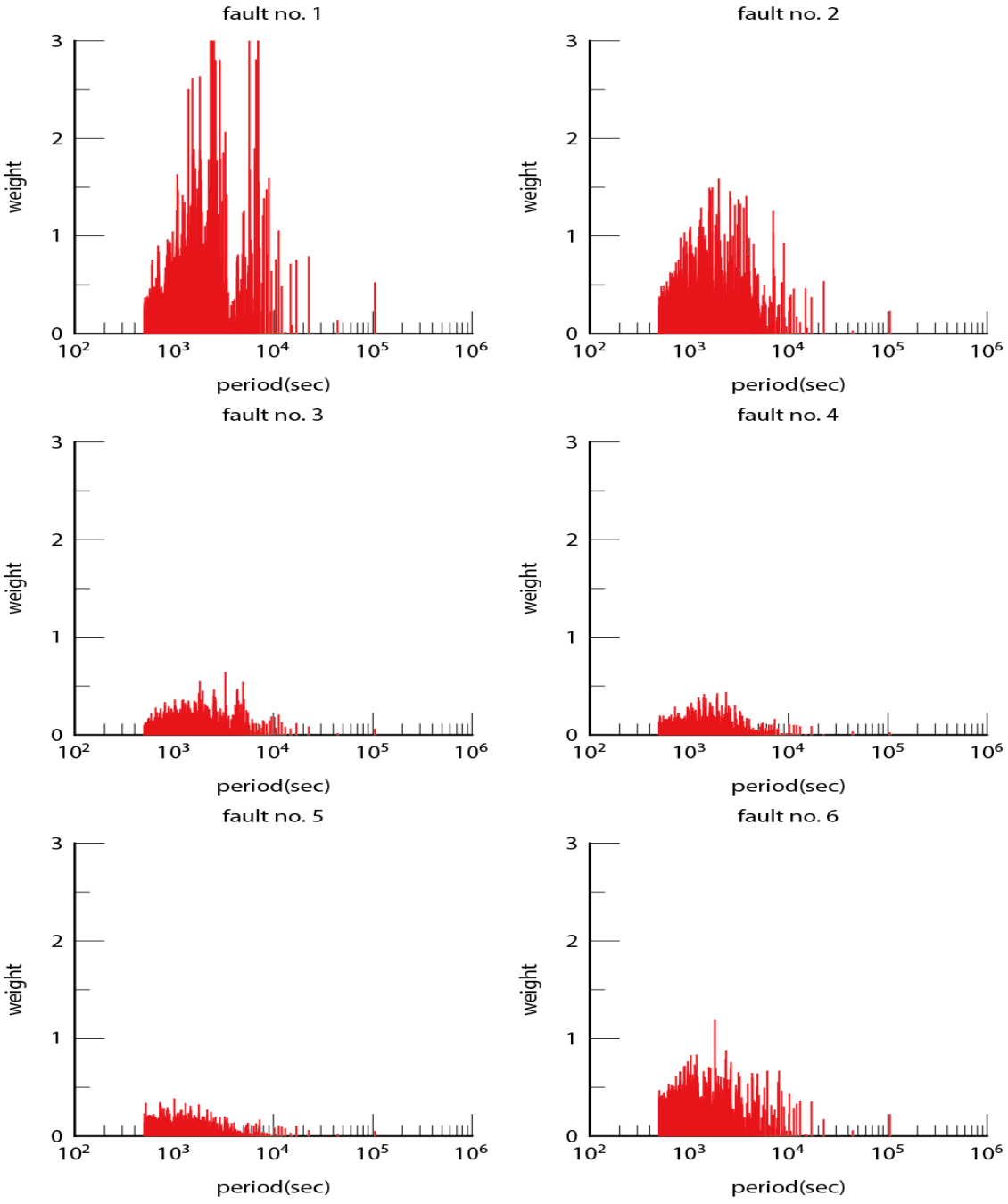

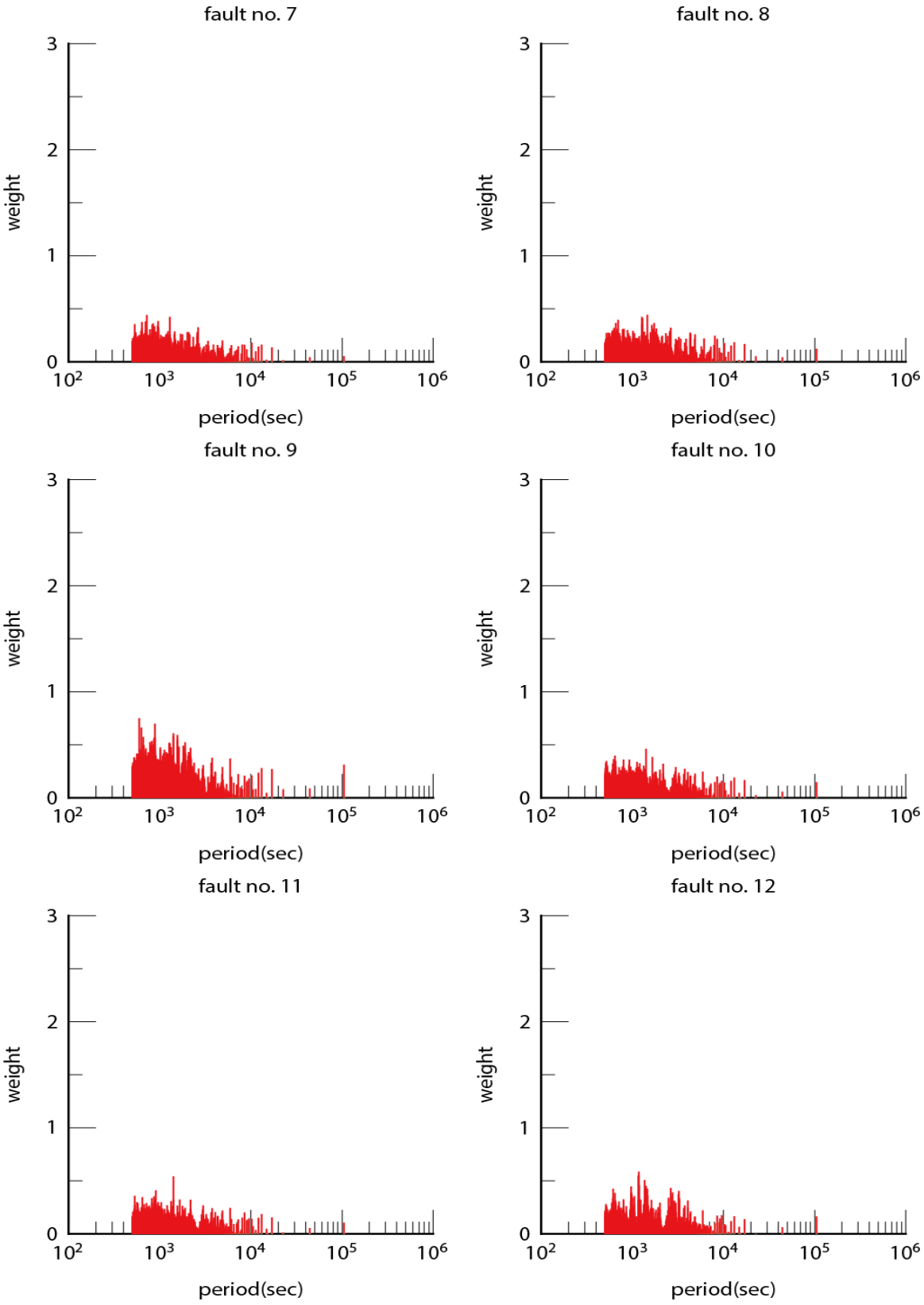
fault no. 7
fault no. 8
fault no. 9
fault no. 10
fault no. 11
fault no. 12
weight
period(sec)
0
1
2
3
10^2
10^3
10^4
10^5
10^6

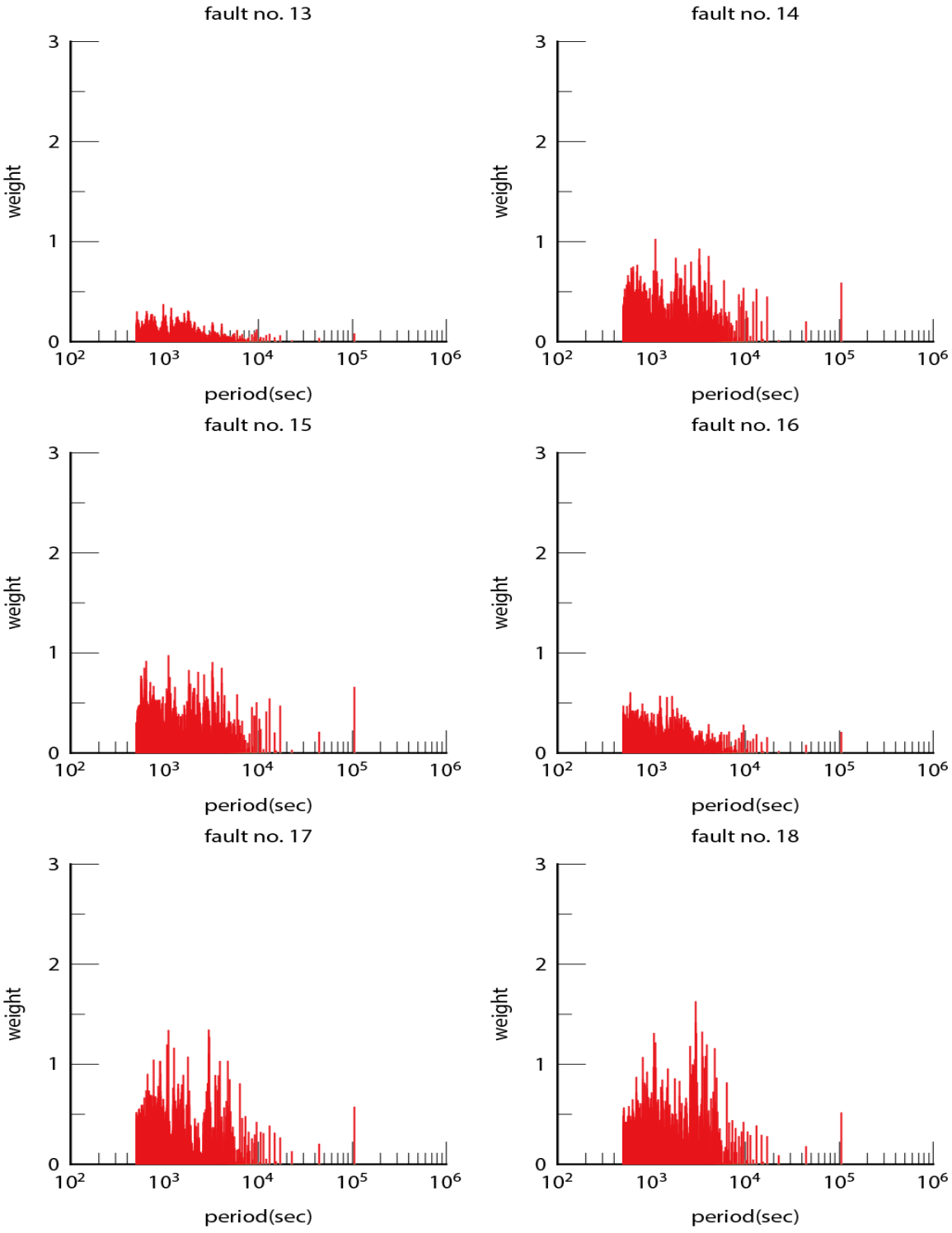
fault no. 13
fault no. 14
fault no. 15
fault no. 16
fault no. 17
fault no. 18
weight
period(sec)
0
1
2
3
10^2
10^3
10^4
10^5
10^6

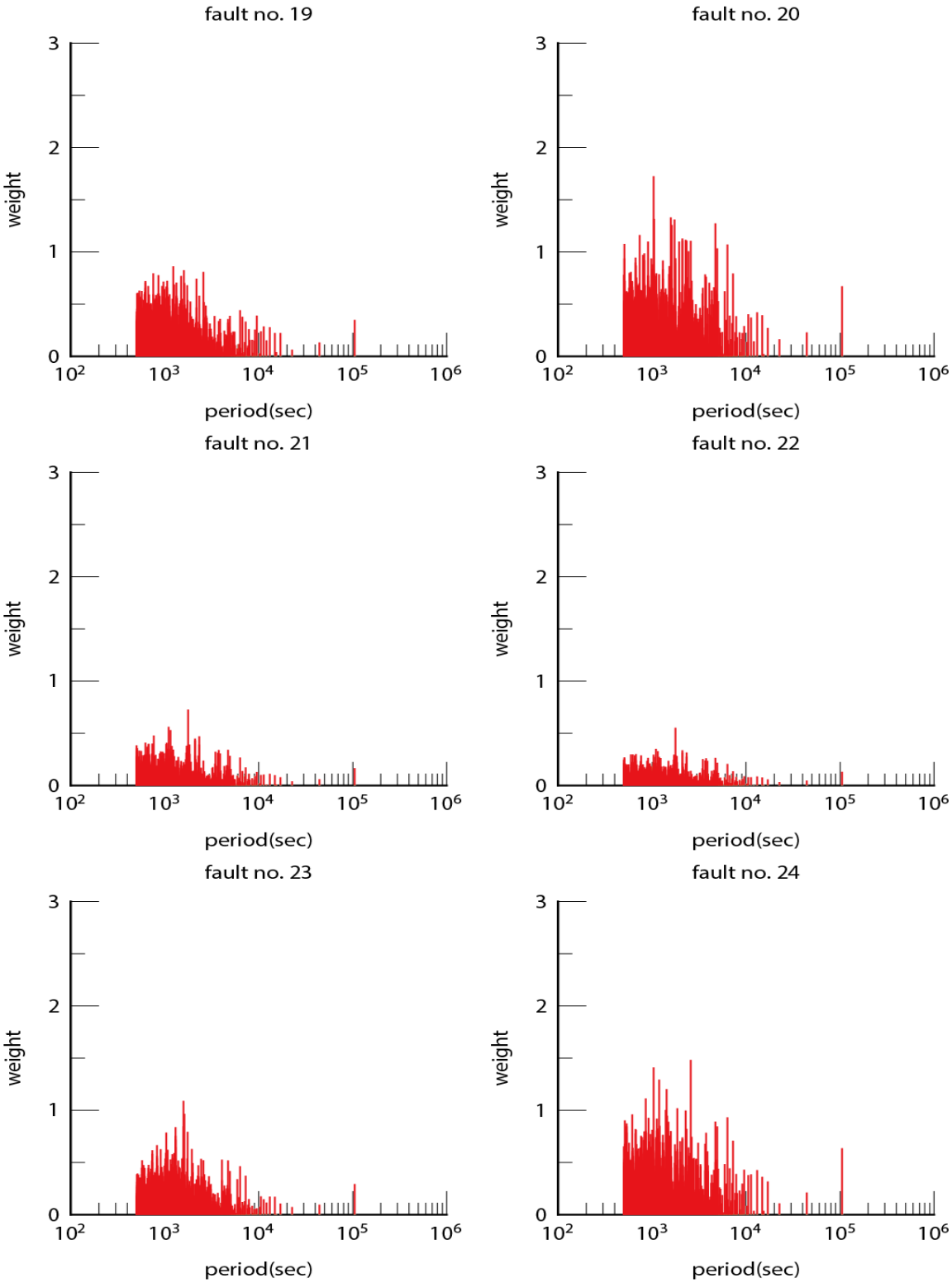
fault no. 19
fault no. 20
fault no. 21
fault no. 22
fault no. 23
fault no. 24
weight
period(sec)
0
1
2
3
10^2
10^3
10^4
10^5
10^6

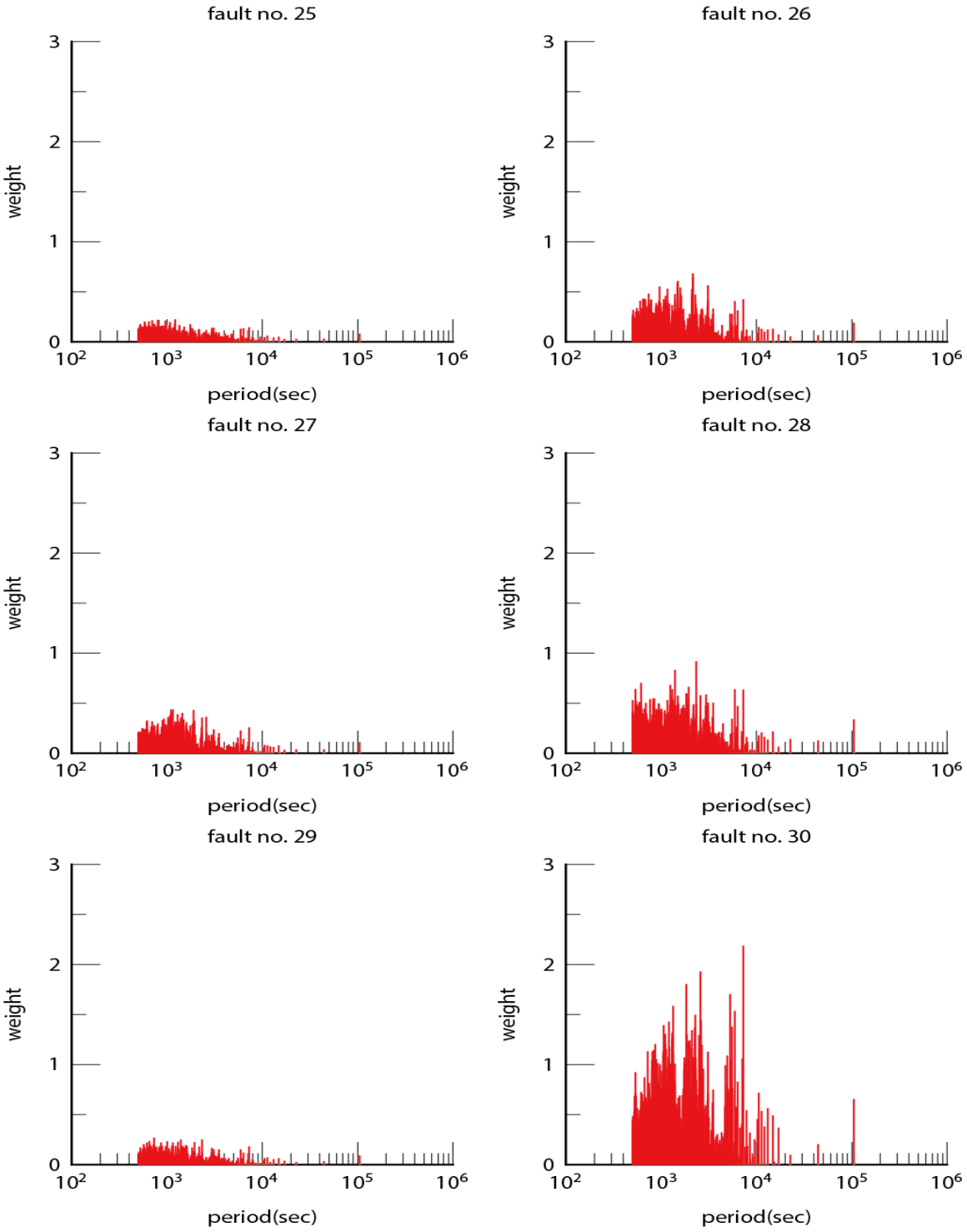
fault no. 25
fault no. 26
fault no. 27
fault no. 28
fault no. 29
fault no. 30
weight
period(sec)
0
1
2
3
10^2
10^3
10^4
10^5
10^6

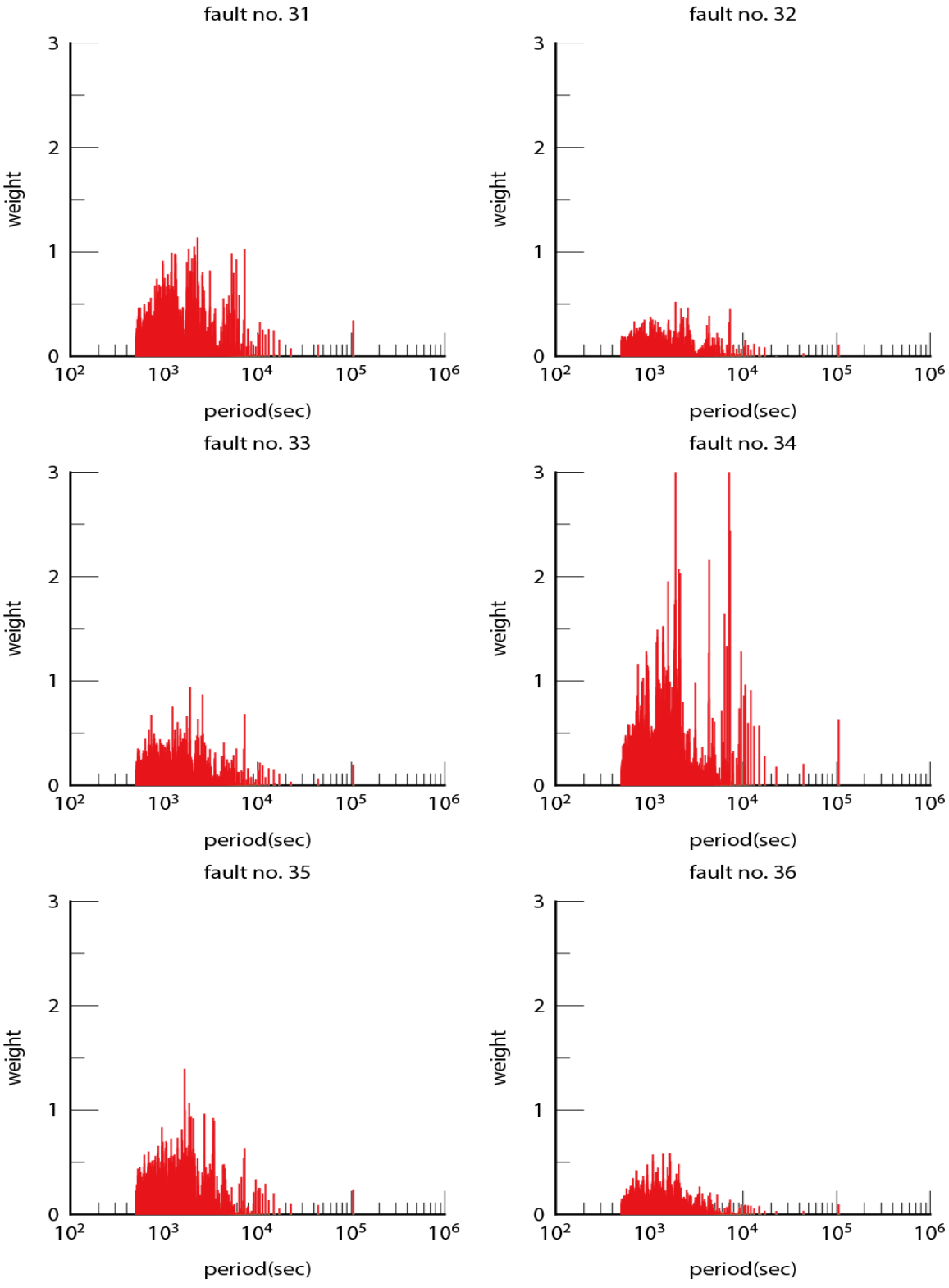
fault no. 31
fault no. 32
fault no. 33
fault no. 34
fault no. 35
fault no. 36
weight
period(sec)
0
1
2
3
10^2
10^3
10^4
10^5
10^6

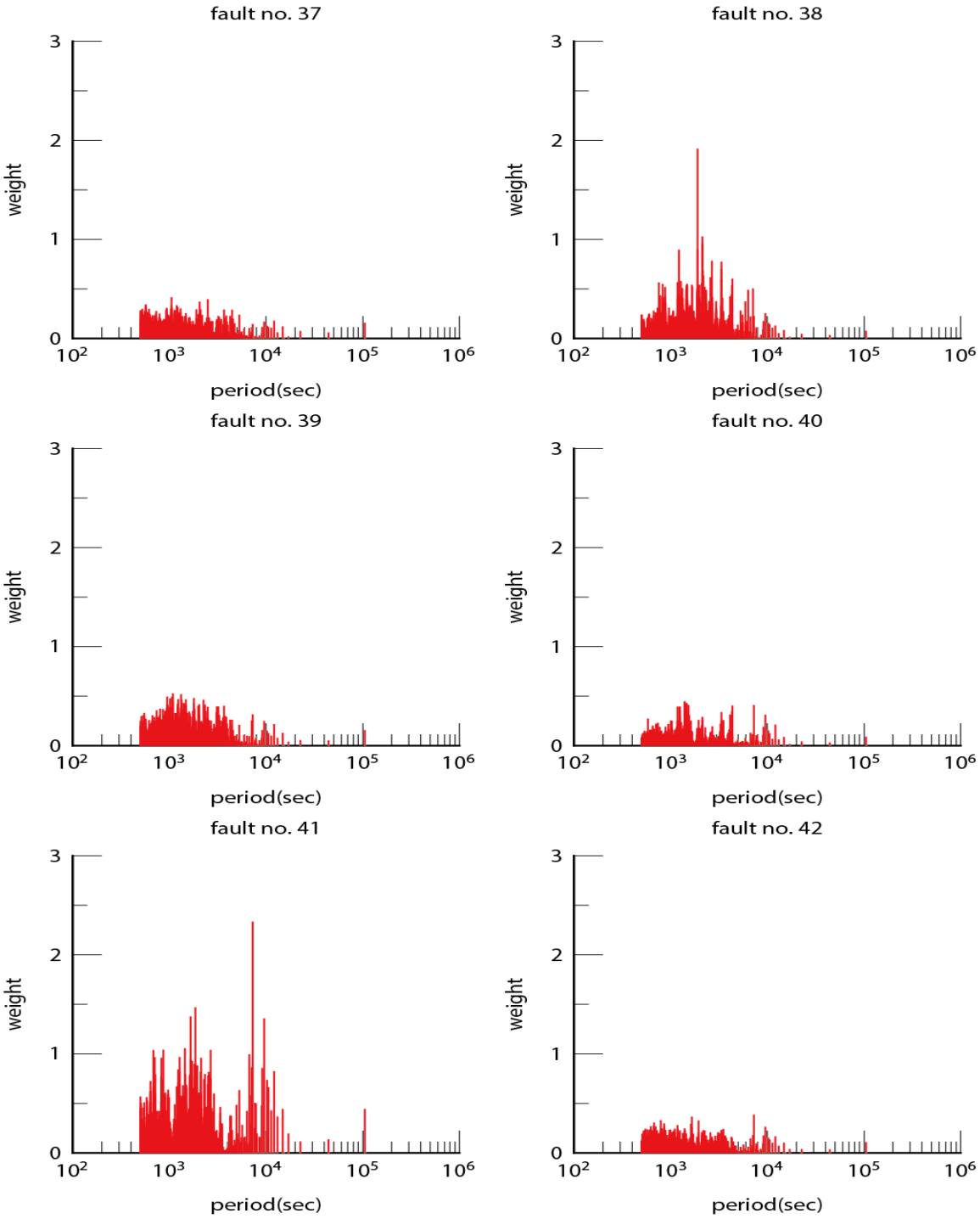
fault no. 37
fault no. 38
fault no. 39
fault no. 40
fault no. 41
fault no. 42
weight
period(sec)
0
1
2
3
10^2
10^3
10^4
10^5
10^6

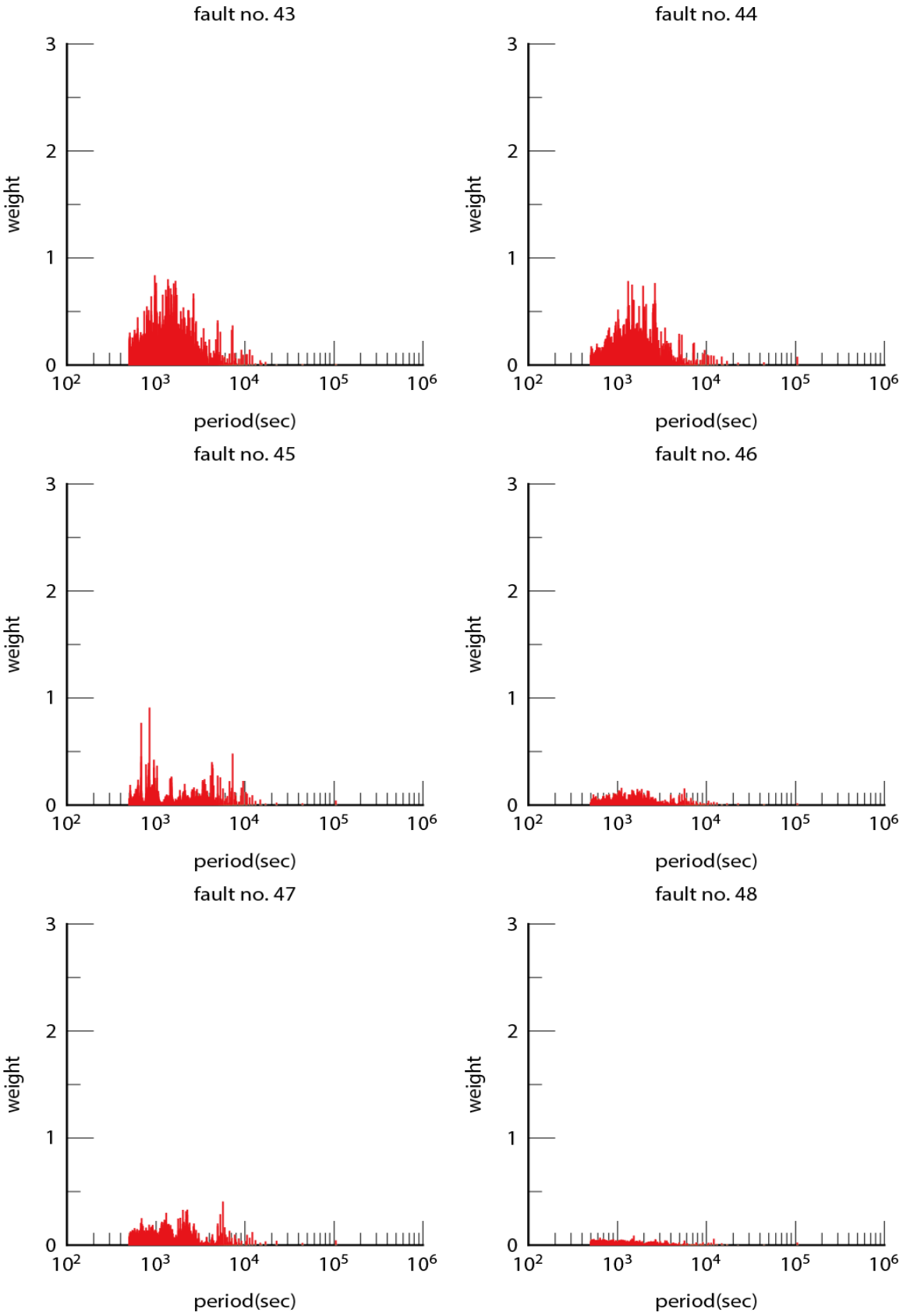
fault no. 43
fault no. 44
fault no. 45
fault no. 46
fault no. 47
fault no. 48
weight
period(sec)
0
1
2
3
10^2
10^3
10^4
10^5
10^6

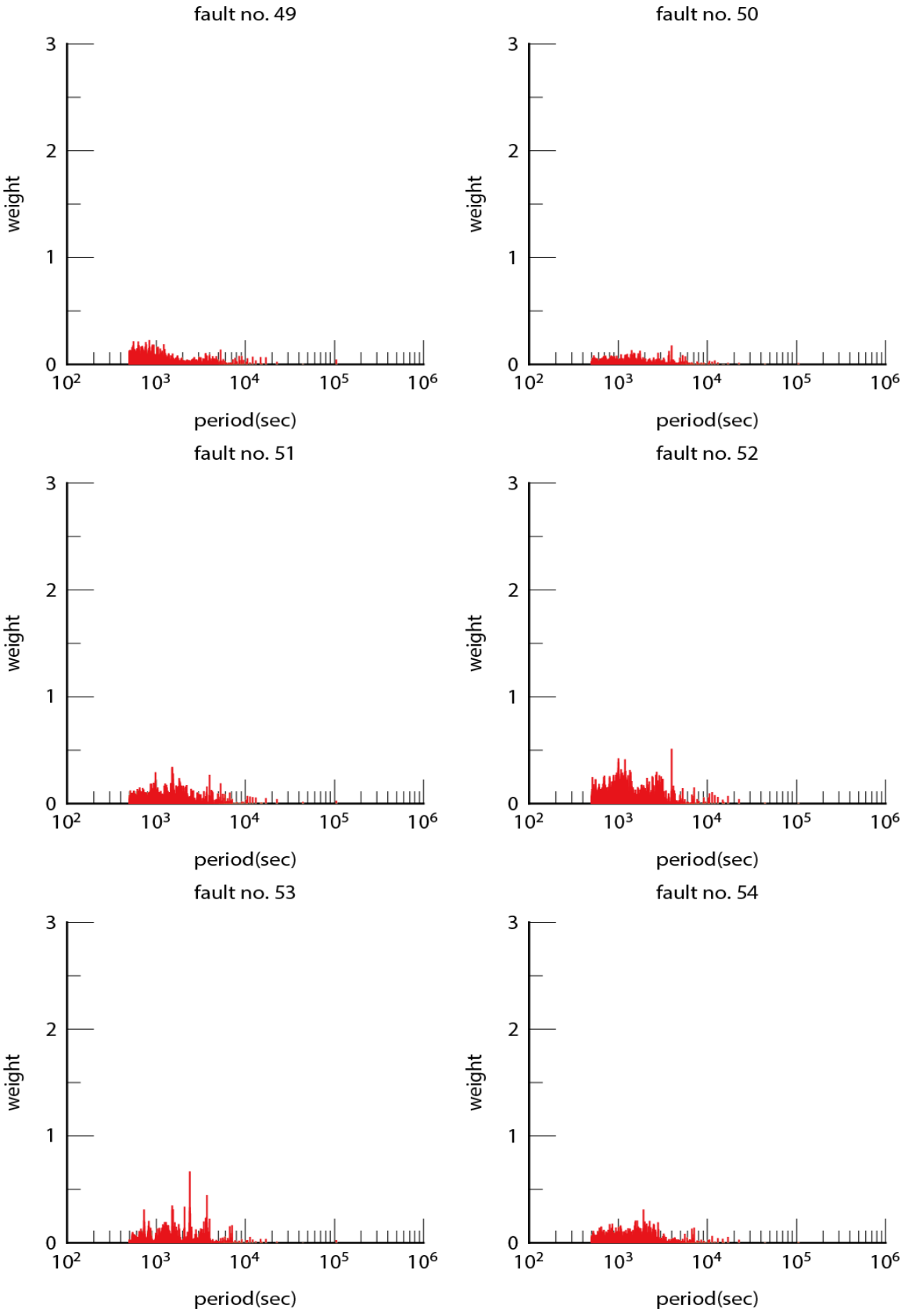
fault no. 49
fault no. 50
fault no. 51
fault no. 52
fault no. 53
fault no. 54
weight
period(sec)
0
1
2
3
10^2
10^3
10^4
10^5
10^6

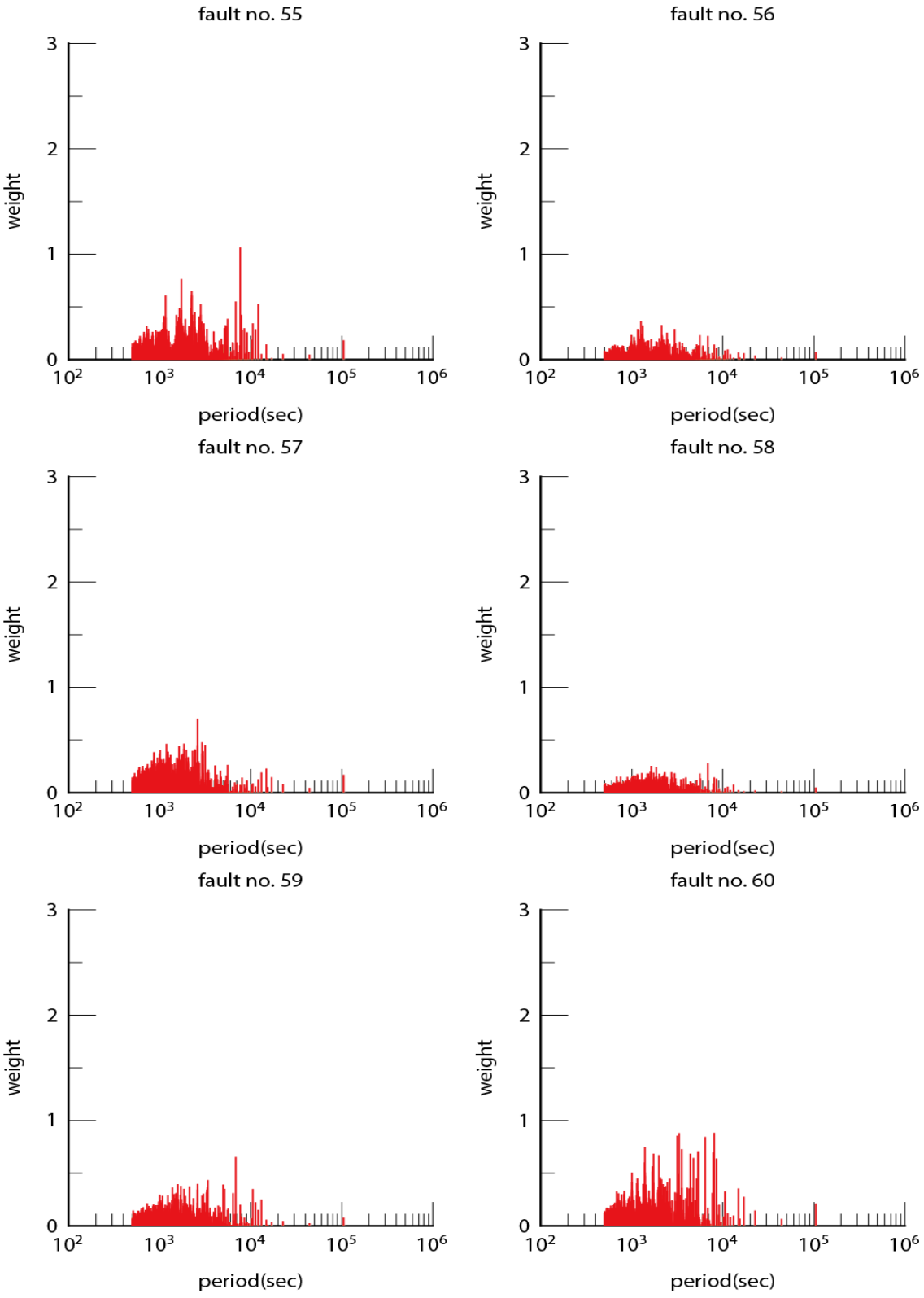
fault no. 55
fault no. 56
fault no. 57
fault no. 58
fault no. 59
fault no. 60
weight
period(sec)
0
1
2
3
10^2
10^3
10^4
10^5
10^6